NASA Technical Memorandum 4562

Hypersonic Vehicle Model and Control Law Development Using H_∞ and μ Synthesis

Irene M. Gregory
Langley Research Center • Hampton, Virginia

Rajiv S. Chowdhry
Lockheed Engineering & Sciences Company • Hampton, Virginia

John D. McMinn and John D. Shaughnessy
Langley Research Center • Hampton, Virginia

National Aeronautics and Space Administration
Langley Research Center • Hampton, Virginia 23681-0001

October 1994

This publication is available from the following sources:

NASA Center for AeroSpace Information
800 Elkridge Landing Road
Linthicum Heights, MD 21090-2934
(301) 621-0390

National Technical Information Service (NTIS)
5285 Port Royal Road
Springfield, VA 22161-2171
(703) 487-4650

Contents

Symbols

a	bandwidth of elevon dynamics, 30 rad/sec
b	bandwidth of fuel flow rate dynamics, 100 rad/sec
C	set of complex numbers
$\mathbf{D}$	positive definite Hermitian matrix
d	exogenous inputs, (i.e., noise, commands, turbulence)
d'	generalized exogenous input, $d' = [z\ d]$
e	error/performance
e'	generalized output performance $e' = [w\ e]$
$F_l(P, K)$	closed-loop response between e' and d'
$F_u(G, \Delta)$	perturbed closed-loop response between e and d
F_u, F_w	longitudinal and vertical Dryden turbulence filters
f	stoichiometric ratio for hydrogen, 0.029
$G(s)$	augmented system plant that contains $K(s)$ and $P(s)$
H_∞	Banach space consisting of functions $F(s)$ which are analytic in Re $s > 0$, take values in $\mathbf{C}^{n \times m}$, and are bounded in Re $s > 0$
h	altitude, ft
I_n	$n \times n$ identity matrix
$K(s)$	controller
M	Mach number
$\dot{m}_a$	air mass flow rate, slugs/sec
$\dot{m}_f$	fuel mass flow rate, slugs/sec
$P(s)$	generalized plant structure
$\mathbf{Q}$	unitary matrix
q	pitch rate, deg/sec
Re	real part
s	variable of Laplace multiplier
u	control effectors variable
V	velocity, ft/sec
W_{noise}	measurement noise weighting matrix
$W_p[\ \cdot\ ]$	performance weighting matrix for given variable
W_Δ	uncertainty weighting matrix
w	uncertainty matrix input variable
w_i	unity magnitude white Gaussian noise with zero mean
X_{noise}	state measurement noise variable
x	state longitudinal variable
y	sensed variable
z	uncertainty matrix output variable
α	inertial angle of attack, deg
β	peak magnitude of frequency response
Δ	uncertainty matrix
Δt	time increment
$\boldsymbol{\Delta}$	general set of complex perturbations not restricted by bounds
$\Delta\delta e, \Delta\delta\dot{m}_f$	uncertainty in control effectors
δe	symmetric elevon, deg
$\delta e_c, \delta\dot{m}_{f,c}$	controller-commanded control inputs
$\delta e_{\text{eff}}, \delta\dot{m}_{f,\text{eff}}$	effective control inputs
$\tilde{\delta}e_c, \tilde{\delta}\dot{m}_{f,c}$	uncertainty matrix inputs in general structure
η	fuel equivalence ratio
θ	pitch angle, deg
μ	structured singular value
$\bar{\sigma}$	maximum singular value

Abbreviations:

DOF	degree of freedom
iff	if and only if
LTI	linear time invariant
SSTO	single stage to orbit

Notation:

$[\,\cdot\,]_p$	performance-weighted variables
$[V, h]_c$	commanded velocity and altitude
$[V, h]_{ep}$	performance-weighted velocity and altitude error
$\|\cdot\|_\infty$	infinity norm
$\|\cdot\|_\mu$	maximum structured singular value over all frequency ω
$\sup\limits_{\omega}$	least upper bound over all frequency ω

A dot over a symbol indicates differentiation with respect to time.

Introduction

Single-stage-to-orbit (SSTO) air-breathing vehicles present significant challenges in many technological areas and especially in flight control. These vehicles traverse a broader flight envelope than any aircraft flown to date and performance is critical throughout the entire flight regime to achieve the mission objective. Large variations in vehicle static and dynamic characteristics and in mass properties, such as significant movement of the aerodynamic center of pressure, result in continuously changing static stability margins throughout the flight envelope. (See ref. 1.) Furthermore, an additional source of uncertainty arises from the accuracy of mathematical dynamic models used to describe the vehicle in control system design. These challenges and the limited availability of empirical data above a Mach number of 8 in aerodynamics, propulsion, aeroelasticity, and heating as well as limited knowledge of their combined effects on vehicle mission performance dictate the need for a robust yet performance-oriented control system.

The airframe/propulsion interactions, possibly the most complex of any vehicle, are critically important to a successful hypersonic vehicle mission. The high sensitivity of the air-breathing propulsion system performance to changes in angle of attack and to dynamic pressure has been identified (ref. 2) and confirmed. (See ref. 1.) Furthermore, atmospheric turbulence and large density variations at a high altitude and at a high Mach number (ref. 3) introduce other significant sources of uncertainty in the performance of an air-breathing propulsion system for the control system.

In addition, such parameter uncertainties as propulsive efficiency, drag, and weight have major effects on performance margins as the vehicle reaches orbital speed. (See ref. 4.) The significantly detrimental effect of control surface deflection-induced drag on fuel consumption to orbit (ref. 5) provides another compelling reason for control system optimization in hypersonic vehicles.

These issues and their impact on control system development have been recognized by numerous researchers. (See refs. 1, 6, and 7.) The control work in this area has primarily addressed an air-breathing hypersonic cruiser (ref. 7), which assumes equilibrium steady-state flight with changes in the coefficients of the equations of motion stemming from poor model description rather than from changing flight parameters due to acceleration. Furthermore, the control laws developed for the ascent phase have either disregarded the impact of angle-of-attack variations on air-breathing propulsion performance (ref. 7) or, while addressing tracking and atmospheric turbulence issues, did not explicitly consider performance robustness. (See ref. 8.)

Recent application of modern robust control theory to Space Shuttle (ref. 9) and fighter airplane (ref. 10) flight control problems demonstrated potential benefits to the above challenges. The objective of this research is twofold: to assess applicability and to exploit the capability of modern multivariable robust control theory to explicitly deal with performance and with the uncertainty arising from changing flight conditions and vehicle characteristics. The problem is formulated to deal with the challenges associated with an SSTO vehicle and air-breathing propulsion system. A structured uncertainty model, representing parametric variations as actuator uncertainty, is used to illustrate the distinction between two modern design procedures, H_∞ and μ synthesis.

In the first section of this paper is a brief review of robustness measures. The issue of possible conservative solutions to some practical problems is discussed and the structured singular value is introduced. The theoretical basis for the two synthesis procedures is also provided. In the next section is the derivation of a five-state longitudinal linear model description from an ascent trajectory of a conical accelerator vehicle. After that is the problem description of the uncertainty model, the H_∞ weighting function selection, and the explicit inclusion of stochastic atmospheric turbulence in a controller design. The last section deals with the application of H_∞ and μ controller synthesis and analysis techniques. The conclusions derived from this study follow. Appendixes A E provide further details of the hypersonic vehicle model and controller design. Included in the appendixes are an updated scramjet propusion model, the derivation of linear models from points along a continuous-acceleration flight trajectory, an atmospheric model implementation in the design and simulation, and the numerical values of the original plant and the derived controllers.

Theoretical Review of μ

This section provides essential theorems for robustness and performance analysis in a system with uncertainty. Far more detailed and rigorous discussion is presented in references 11 13.

Analysis methods based on singular values have been successful in providing multiloop extensions for classical single-loop techniques. (See ref. 11.) However, these methods are limited to providing necessary and sufficient conditions for robust stability for systems with unstructured uncertainty, defined as norm-bounded but otherwise unknown perturbations. Consider, for example, the standard problem of analyzing a feedback system with simultaneous multiplicative uncertainty at the plant input and output signals. To apply singular value techniques, both perturbations must be reflected to a single location in the feedback loop, thus immediately inducing conservatism. However, because the combination of linear transformations is linear, any uncertainty occurring at several different locations in the feedback loop can be rearranged as a single block-diagonal perturbation in a larger feedback loop. In other words, even unstructured uncertainty at the loop component level becomes highly structured at the system level. (From MUSYN: Robust Multivariable Control Short Course and Software, available from John C. Doyle, Andrew Packard, and Gary Balas, MUSYN, Inc., Minneapolis, Minnesota.)

The general framework for the robust control problem is introduced in figure 1(a). Any linear combination of inputs, outputs, commands, perturbations, and controller can be arranged into the form in the diagram. (See ref. 12.) Furthermore, the exogenous inputs d, the perturbation Δ, and the output error e are normalized to 1 with all weightings and scalings absorbed into the generalized plant structure P. This arrangement results in unit invariant conditions for robust stability and performance expressed in terms of μ that are presented later in this section. For the analysis the controller K can be considered an element of a larger plant G and can be absorbed along with the generalized plant P into its structure. The diagram for the analysis reduces to that in figure 1(b). The analysis problem itself involves determining whether e remains in a desired set for sets of d and Δ. The resulting structure of G can be partitioned as

$$\begin{bmatrix} w \\ e \end{bmatrix} = \begin{bmatrix} G_{11} & G_{12} \\ G_{21} & G_{22} \end{bmatrix} \begin{bmatrix} z \\ d \end{bmatrix} \tag{1}$$

Closing the upper loop of G with the uncertainty matrix Δ results in a linear fractional transformation given by

$$e = F_u(G, \Delta)d = \left[G_{22} + G_{21}\Delta(I - G_{11}\Delta)^{-1}G_{12}\right]d \tag{2}$$

The structure for synthesis is similarly given in figure 1(c). The inputs and outputs associated with Δ are absorbed into the exogenous input d' and error e'. The equation relating the generalized inputs to outputs is given by

$$e = F_l(P, K)d' = \left[P_{11} + P_{12}K(I - P_{22}K)^{-1}P_{21}\right]d' \tag{3}$$

The conditions for stability and performance expressed in terms of H_∞ bounds on portions of the generalized plant are given and discussed in some detail in references 12 and 13. In the absence of uncertainty, the nominal performance objectives are expressed in terms of

$$\|G_{22}\|_\infty \equiv \sup_\omega \bar{\sigma}[G_{22}(j\omega)] \leq 1 \tag{4}$$

which relates the response $e(\|e\|_2 \leq 1)$ to the set of exogenous inputs $d(\|d\|_2 \leq 1)$. In practice, the use of scalings and weightings is necessary to represent and normalize the varying frequency and spatial content of input and output sets.

Consider plant perturbations that can destabilize a nominally stable system. Robust stability is satisfied for unstructured uncertainty if and only if the following condition holds:

$$\|G_{11}\|_\infty \leq 1 \qquad (\text{for all } \Delta, \bar{\sigma}(\Delta) < 1) \tag{5}$$

In general for practical problems, the uncertainty consists of parameter variations and multiple norm-bounded perturbations that result from the unmodeled system dynamics. Parameter variations often arise from changing flight conditions and represent changes in the coefficients of the equations that describe the physical system. Unfortunately, the norm-bounded test is insufficient and inadequate in dealing with robust performance and with realistic models of plant uncertainty that involve structure.

To handle bounded structured uncertainty, the structured singular value concept and the function μ are used to develop necessary and sufficient conditions. (See ref. 13.) Because any linear problem can be rearranged into the form presented in figure 1(a), the uncertainty Δ will be a member of the set defined as

$$\begin{aligned} \Delta = \Big\{&\mathrm{diag}(\delta_1, \delta_2, \ldots, \delta_m, \Delta_1, \Delta_2, \ldots, \Delta_n) | \delta_i \in \mathbf{C}, \\ &\times \Delta_j \in \mathbf{C}^{k_j \times k_j}\Big\} \end{aligned} \tag{6}$$

and its bounded subset

$$\mathbf{B\Delta} = [\Delta \in \mathbf{\Delta} | \bar{\sigma}(\Delta) < 1] \tag{7}$$

where prefix **B** denotes a unit ball. The function μ is defined as

$$\mu(M) \equiv \frac{1}{\min\limits_{\Delta \in \Delta} [\bar{\sigma}(\Delta) | \det(I - M\Delta) = 0]} \qquad \left(\text{for } M \in \mathbf{C}^{n \times n}\right) \tag{8}$$

unless no $\Delta \in \boldsymbol{\Delta}$ makes $I + M\Delta$ singular, in which case $\mu(M) = 0$. Based on the definition of μ and its properties, the robust stability condition for structured uncertainty is derived. Robust stability is satisfied if and only if

$$\|G_{11}\|_{\mu} \equiv \sup_{\omega} \mu[G_{11}(j\omega)] \leq 1 \qquad (\text{for all } \Delta \in \mathbf{B\Delta}) \quad (9)$$

Note that, in contrast to $\bar{\sigma}$, the value of μ depends on G_{11} as well as on the structure of the perturbations Δ. In addition, the properties of μ permit the robust stability of a system with $\|G_{11}\|_{\mu} = \beta$ to be maintained for all.

The question of interest to the control designer is how well the system performs in the presence of uncertainty. Consider the issue of robust performance, which describes performance with noise and perturbations occurring simultaneously. Thus, $F_u(G, \Delta)$ is stable and

$$\|F_u(G,\Delta)\|_{\infty} \leq 1 \qquad \Big(\text{for all } \Delta \in \ \mathbf{B\Delta}\text{iff } \|G\|_{\mu} \leq 1\Big) \quad (10)$$

The definition of μ is typically not very useful in μ computation; however, the extreme cases for the structure of Δ provide the basis for the computational bounds on μ. In these special cases in which Δ belongs to one of the extreme sets described below, μ is exactly either the spectral radius or the maximum singular value

$$\begin{aligned} \Delta &= \{\delta_i I_n \mid \delta \in \mathbf{C}\} \rightarrow \mu(G) = \rho(G) \\ \Delta &= \mathbf{C}^{n \times n} \rightarrow \mu(G) = \bar{\sigma}(G) \end{aligned} \qquad (11)$$

Combining these special cases with the fact that μ is invariant under scaling gives the bounds on μ. Let $\mathbf{D}$ and $\mathbf{Q}$ be the scaling matrices belonging to the set defined as given by

$$\begin{aligned} D &= \{\text{diag}(D_1, \ldots, D_m, d_1 I, \ldots, d_n I) : D_i = D_i^H > 0, d_j > 0\} \\ Q &= \{Q \in \boldsymbol{\Delta} : Q^H Q = I_n\} \end{aligned} \qquad (12)$$

Then the bounds on μ are

$$\max_{Q \in \mathbf{Q}} \rho(QG) \leq \mu(G) \leq \inf_{D \in \mathbf{D}} \bar{\sigma}\Big(DGD^{-1}\Big) \qquad (13)$$

The structure of Δ in general consists of repeated scalar and full matrix blocks. The measure μ can be computed exactly from the upper bound if the structure of Δ corresponds to $2S + F \leq 3$, where S is the number of repeated scalar blocks and F is the number of full blocks. Thus,

$$\mu(G) = \inf_{D \in \mathbf{D}} \bar{\sigma}\Big(DGD^{-1}\Big) \qquad (14)$$

For the problem considered in this paper, Δ consists of a single repeated scalar block and is given in a later section. The transformation DGD^{-1} is essentially a scaling of the inputs and outputs of G and does not change the value of μ, as mentioned above. In addition, because μ can be computed exactly as $\bar{\sigma}$ plus scaling, the methods developed for H_{∞} optimal control can be used to optimize μ.

The μ analysis can be combined with the H_{∞} optimal control to produce μ synthesis to provide H_{∞} performance in the presence of structured uncertainty. The scaling matrices D and D^{-1} are used to reflect the structure of Δ over the frequency range. The problem now becomes reformulated as an H_{∞}-norm minimization,

$$\|DF_l(P,K)D^{-1}\|_{\infty} \leq 1 \qquad (15)$$

known as D K iteration. As the D K name implies, the μ synthesis approach is to iterate between D and K until the solution converges. (See ref. 13.) The method is not guaranteed to produce a global minimum or to converge; however, the results, widely published in the literature, have been successful in practical applications.

Hypersonic Vehicle Model

A conical accelerator configuration was the example for a generic air-breathing hypersonic vehicle. (See ref. 14.) The mathematical model associated with the aerodynamic forces and moments, propulsion system, and rigid-body mass moments of inertia for this vehicle are given in reference 14. An updated version of the propulsion model is used in this study and is described briefly in appendix A. As the vehicle accelerated through a Mach number of 8 at an altitude of 85 700 ft, a 10-state linear model representing the vehicle dynamics was obtained at this nonequilibrium flight condition, which is characterized by nonzero translational and rotational accelerations. The conceptual methodology for numerical derivation of the linear time-invariant models from the six-degree-of-freedom simulation is described in appendix B. The linear model was decoupled into a five-state longitudinal and a five-state lateral-directional model. The five-state longitudinal variable x and control effector u utilized in this study are given by

$$x = \begin{bmatrix} V \\ \alpha \\ q \\ \theta \\ h \end{bmatrix} \qquad (16)$$

$$u = \begin{bmatrix} \delta e \\ \delta \dot{m}_f \end{bmatrix} \tag{17}$$

The state and control variables are perturbation quantities and represent deviations from nominal flight conditions. The nominal flight conditions and trim accelerations are provided for reference in table I. The open-loop characteristics of the plant are unstable. The eigenvalues are as follows:

Open-Loop Eigenvalues

6.5403×10^{-3}

$-9.134 \times 10^{4} \pm j3.5576 \times 10^{-2}$

-1.8312

1.6533

Note that the altitude is included as a state variable to account for temperature, density, and gravity gradients. These variations significantly affect the longitudinal long-period dynamics of the vehicle and add an aperiodic altitude mode caused by the variation of atmospheric density with altitude. (See ref. 15.)

Several interesting nuances about this model are worth considering. In all practical problems, a linear time invariant (LTI) system is only an approximation for the real physical system. In most cases, time invariance of system characteristics is valid for small increments of time dictated by the problem. In this particular case, the vehicle accelerates through a Mach number of 8 and the LTI system is valid for only that instant. However, if the parameter variation with time is represented as a multiplicative uncertainty such that $\tilde{G} = G(I + \Delta)$, then the linear system can be considered time invariant over some interval and can be used in LTI control design. In this initial application of the H_∞ and μ control theories, all uncertainty is assumed to be represented by individual uncertainty on the effectiveness of the elevon and the fuel flow rate. This representation fulfills two desirable guidelines—it keeps the initial application uncomplicated and it introduces structured uncertainty into the problem.

The second important point is fuel equivalence ratio as a control effector. The fuel equivalence ratio η is defined as

$$\eta = \frac{\dot{m}_f}{f \dot{m}_a} \tag{18}$$

where $\dot{m}_f$ is the fuel mass flow rate, f is the stoichiometric ratio that for hydrogen is 0.029, and $\dot{m}_a$ is the air mass flow rate. In practice, it is important to recognize that $\dot{m}_a$ changes almost instantaneously at hypersonic speeds with a change in angle of attack. The original nonlinear model assumes that $\dot{m}_a$ is an instantaneously adjustable quantity and thus is kept constant with changing flight conditions, which results in $\%\Delta\eta = \%\Delta\dot{m}_f$. Therefore, to reflect realistic utilization and to forgo time-consuming changes in the nonlinear model, the control problem is formulated with the fuel flow rate as the control effector and its changes are presented as the percentage of change from the nominal rather than as actual units of mass per second.

The dependence of inlet conditions on angle-of-attack variation is not explicitly included in the nonlinear model. However, the control problem is formulated to consider the major aerodynamic/propulsive interactions. These interactions are reflected in explicit performance requirements on angle of attack as well as on the engine control effector $\delta\dot{m}_f$, rather than on the fuel equivalence ratio. Using η as a control effector implies that either the angle of attack has no effect on $\dot{m}_a$ flow into the propulsion system or that $\dot{m}_a$ is instantaneously measurable, thus allowing for matching adjustment to $\dot{m}_f$ to get the desired η. However, neither implication is realistic. Hence, in practice, while the system is following a commanded η, $\delta\dot{m}_f$ must be used as a control effector.

Robust Control Problem Formulation

The controller requirements were established based on the near-optimal ascent trajectory and on the sensitivity of the air-breathing propulsion system to angle-of-attack variations. Thus, the specifications in the presence of atmospheric turbulence and system uncertainty are the following: highly accurate tracking of velocity and altitude commands, limiting angle-of-attack total deviation to ≈0.5° from nominal, minimizing control power use, and stabilizing the vehicle. For this study, $x_{\text{state}} = y_{\text{meas}}$ was assumed available for output feedback; the assumption was based on the availability of inertial angle-of-attack calculations with feedback from an inertial measurement unit (IMU). The reason for inertial angle of attack is twofold. First, a conventional angle-of-attack measurement that uses a pitot tube in a free stream is not practical at hypersonic speeds because of very high stagnation temperatures. Second, angle-of-attack perturbations from atmospheric turbulence are significant compared with the desired response (≈20 percent); a signal of such magnitude should not be introduced directly into the feedback loop. Measuring the aerodynamic angle of attack would introduce atmospheric turbulence into the control problem as measurement noise rather than as a disturbance, thus changing the way it would be handled by the control law.

The block diagram problem formulation is illustrated in figure 2(a). All feedback state measurements were assumed corrupted by noise. The noise matrix W_{noise} was represented by

$$W_{\text{noise}} = 10^{-6} I_5 \tag{19}$$

The noise matrix was only partly intended to represent realistic sensor data; rather, it was included to satisfy current computational requirements associated with solving the H_∞ problem. The control actuator dynamics were represented by first-order filters with a 30 rad/sec bandwidth for the elevon and a 100 rad/sec bandwidth for the fuel flow rate. In a generic air-breathing hypersonic vehicle, the uncertainty, as discussed in the "Introduction," comes from different sources and occurs simultaneously. Thus, the physics of the problem imposes a structure on the uncertainty of a hypersonic vehicle. For this problem, system uncertainty due to parameter variation arising from vehicle acceleration was represented as variations in the effectiveness of the commanded elevon and the fuel flow rate. Specifically, a 20-percent multiplicative uncertainty in control effectiveness was introduced where

$$\Delta = \begin{bmatrix} \delta & 0 \\ 0 & \delta \end{bmatrix} \qquad (\delta \in \mathbf{C} \| \Delta \|_\infty \leq 1) \tag{20}$$

and the uncertainty weighting matrix W_Δ was

$$W_\Delta = \begin{bmatrix} 0.20 & 0 \\ 0 & 0.20 \end{bmatrix} \tag{21}$$

Thus, the control effectiveness was forced to vary from 80 to 120 percent of the assumed nominal value. At this stage of problem development, atmospheric density perturbations were assumed reflected in the 20-percent uncertainty in fuel flow rate effectiveness.

Performance specifications for a flight control system translate quite well into an H_∞ context for this problem. In designing for tight performance margins, performance weighting functions were augmented to the system. Performance specifications for H_∞ make practical sense only when meaningful variables are specified for weighting functions. As illustrated in figure 2(a), the weighting functions for control effector positions and rates as well as for the state vector were employed as output performance variables.

Specific performance requirements were derived from a near-optimal fuel ascent trajectory for the conical accelerator. Thus, frequency dependent performance weightings are used for velocity and altitude errors. Such time history requirements as percentage of overshoot, steady-state error, and response time constant are translated into first-order transfer functions given by equations (22) and (23). The details for deriving these transfer functions as well as for other performance weightings are given in appendix C. Thus, the velocity performance is specified by

$$W_p V_c = \frac{0.5(s + 4.330 \times 10^{-2})}{s + 2.165 \times 10^{-4}} \tag{22}$$

Similarly, altitude response is constrained by

$$W_{ph_c} = \frac{0.5(s + 3.849 \times 10^{-2})}{s + 1.925 \times 10^{-4}} \tag{23}$$

The performance weightings on velocity and altitude describe the response of each variable to the commanded value and to the ability to reject disturbances. Low-frequency gain describes both the steady-state error and the magnitude of disturbance rejection, which is discussed in more detail in appendix C. Because velocity and altitude were the only variables tracked, constant weighting was applied to angle of attack α, q, and θ, resulting in

$$W_p \begin{bmatrix} \alpha \\ q \\ \theta \end{bmatrix} = \begin{bmatrix} 20 \\ 1 \\ 1 \end{bmatrix} \tag{24}$$

The weighting for α was based on the desire to attenuate atmospheric disturbances and to limit the magnitude of the output as much as possible without violating the performance requirements of other variables. The responses of q and θ, which are indirectly related to α response, were not of primary interest, as reflected in the weighting selection. The actuator position and rate limits were imposed by

$$W_p \begin{bmatrix} \delta e \\ \delta \dot{m}_f \end{bmatrix} = \begin{bmatrix} 30 \\ 60 \end{bmatrix} \tag{25}$$

$$W_p \begin{bmatrix} \delta e \\ \delta \ddot{m}_f \end{bmatrix} = \begin{bmatrix} 20 \\ 10 \end{bmatrix} \tag{26}$$

Atmospheric turbulence is also explicitly included in problem formulation. The primary concern is the effect of turbulence on engine performance. Turbulence can affect performance directly either by changing inlet flow conditions or by exciting actuator controllers; in both cases, the result will be undesirable vehicle angle-of-attack variations. Longitudinal and vertical Dryden turbulence filters are implemented as input weighting functions in the generalized framework (F_u and F_w in figure 2(a)). (See refs. 16 and 17.) Filter inputs w_1 and w_2 to F_u and F_w, respectively, represent white zero-mean unit variance noise signals. The longitudinal Dryden filter output is assumed to act along the velocity vector due to a small angle-of-attack flight condition. The vertical Dryden filter is divided by nominal velocity V_o to give the angle of attack instead of the vertical velocity perturbation.

The block diagram in figure 2(a) can be manipulated into the general framework of figure 1(a) as depicted in figure 2(b). Recall that all the input and output signals of the generalized plant P, except for the control input and measured output, belong to the unity bounded sets with scaling absorbed into P. In this problem the performance weighting functions also served as the scaling factors for the output signal set. Thus, the input labels in figure 2(b) refer to the physical quantities represented by the input and output in figure 2(a). Note that the controller-commanded input data are also, after weighting, the Δ matrix input data and thus define the system uncertainty. For control synthesis, the commands, noise, and atmospheric turbulence (contained in d) and the actuator uncertainty (contained in z) are combined into augmented d as denoted in figure 1(c). The results of the controller design process are discussed in the next section and the numerical results for the state-space problem formulation and controller poles and zeros are provided in appendix D.

Robust Control System Design Results and Evaluation

Three different controllers are designed and evaluated for the problem formulated in the prior section. These controllers include the H_∞ controller designed for a nominal system that contains only measurement noise to corrupt the feedback signal. The second design is again the H_∞ controller designed explicitly to tolerate 20-percent uncertainty in control effectiveness. The final design is a μ controller based on the second H_∞ controller. The designs are individually evaluated and compared for how successfully they provide the desired level of performance in the presence of the prescribed level of uncertainty. The dynamic characteristics of the controllers are given in appendix D.

As the initial step in a controller design, an H_∞ controller for a model with no uncertainty is obtained. The nominal airplane model is derived from the system interconnection shown in figure 2(b) either by deleting the rows and columns of P corresponding to w and z or by setting $W_\Delta = 0$. Frequency domain closed-loop system analyses of this H_∞ controller for nominal performance, robust stability, and robust performance are illustrated in figure 3. Robust stability and robust performance were measured for the structured uncertainty using $\mu(\cdot)$ tests of the appropriate transfer function matrix. (See the section, "Theoretical Review of μ.") The closed-loop system that uses the H_∞ controller satisfies nominal performance requirements for simultaneous inputs of two tracking commands, velocity and altitude, and in the presence of longitudinal and vertical atmospheric turbulence. Recall from equation (4) that nominal performance is satisfied if and only if $\bar{\sigma}[G_{22}(j\omega)] \leq 1$ for all frequencies illustrated in figure 3. Satisfying the nominal performance condition signifies that specified response characteristics are met for the worse possible combination of bounded inputs into the nominal system (i.e., no uncertainty). The lack of robust stability and robust performance in the presence of uncertainties is not surprising here because the uncertainties were not explicitly taken into account. This H_∞ controller is used as the baseline in the subsequent comparisons of controller performance.

The time histories of the closed-loop system response were obtained from a linear simulation in this initial application of H_∞ and μ robust control theories. The linear time simulation was used to translate frequency domain results into the time domain, which is more conducive to evaluating actual physical system performance. As mentioned in the problem formulation, moderate atmospheric turbulence was implemented through longitudinal and vertical Dryden filters. Moreover, for consistent implementation in a discrete simulation environment, the continuous-time Dryden filters were divided by $\sqrt{\text{Nyquist frequency}}$. The atmospheric turbulence implementation is discussed in more detail in appendix E.

The time response of the nominal airplane model to simultaneous commands of a velocity change of 100 ft/sec and an altitude change of 1000 ft in the presence of longitudinal and vertical atmospheric turbulence is presented in figures 4(a)–4(e). These figures also include the μ controller nominal performance that will be discussed later in this section. Both velocity and altitude (figs. 4(a) and (b)), meet the performance requirements derived from tracking a near-optimal fuel trajectory. It is interesting to note that the absence of uncertainty in the controller design did not benefit nominal performance as may have been suspected. The lack of uncertainty in elevon effectiveness made this control surface too sensitive to atmospheric turbulence as reflected in the second-order behavior superimposed on the primary response of the altitude as the commanded value is reached. Even when the altitude variable displays this response, the nominal performance criterion is satisfied. Changing the performance weighting on either the elevon or the altitude does not satisfactorily resolve this problem. The propulsion system effective angle of attack shown in figure 4(c) also fulfills performance specifications for total deviation of ≈0.5°. The elevon total deflection in figure 4(d) is roughly 1.5°, thus limiting control-surface-induced drag. The fuel flow rate shown in figure 4(e) avoids large sudden changes in magnitude, thus minimizing transients in the combustor.

If control surface deflection as well as the magnitude and rate of fuel flow rate can be reduced, vehicle performance will improve. Typically, for an air-breathing SSTO vehicle, the payload fraction is ≈3 percent and the fuel fraction is ≈60 percent. (See ref. 3.) Hence, any improvement in fuel fraction due to reduction in control-surface-induced drag has a potential impact on the consumed fuel that is a large percentage of vehicle weight. Furthermore, the performance of the propulsion system is extremely sensitive to changing conditions in the inlet, combustor, and nozzle; therefore, transients in all parts of the engine should be minimized. The control system minimizes perturbations in the inlet conditions by limiting angle of attack and aids combustion stability with smooth changes in fuel flow rate.

As mentioned, the design goal is to maintain performance with a specified 20-percent control power uncertainty. The baseline 12-state H_∞ controller, discussed above, is used for closed-loop system analysis. Before robust performance can be considered, robust stability must be addressed. As is evident from figure 3, the robust stability requirement is not satisfied by the H_∞ controller for the specified uncertainty. Recall from the section "Theoretical Review of μ" that the closed-loop system is internally stable for all perturbations with magnitude $1/\beta$ where β is the peak magnitude of the frequency response. For a system with inputs normalized to 1, as is done in the H_∞ control problem, $\Delta = 1$ for $1/\beta$. If $\beta > 1$, the implication is that the system is destabilized by a perturbation with a smaller magnitude than the specified uncertainty. The fact that $\mu[G_{11}(j\omega)] = 1.174$ implies that the closed-loop system remains stable only for 17-percent uncertainty in the control effectiveness of both the elevon and the fuel flow rate. The details are elaborated upon in Appendix D. The robust performance is also not satisfied by the H_∞ controller because it requires robust stability as a necessary condition.

An H_∞ controller that is designed with 20-percent uncertainty explicitly included in the system (it is treated as unstructured by H_∞ optimization) does not fulfill performance requirements even for an ideal system. In fact, the nominal performance condition $\|G_{22}\|_\infty \leq 1$ is violated as illustrated in figure 5. Figure 6 provides a sample time response of velocity to a 100 ft/sec step command. The time response clearly shows that the velocity response does not achieve the desired steady-state error (<5 percent) or the rise time (40 sec). In fact, the response to the velocity command violates the nominal performance criterion. Further analysis indicates that either system uncertainty conditions or performance specifications on the tracking variables must be relaxed; otherwise, an H_∞ controller cannot fulfill robust performance requirements as specified for this problem. However, this controller serves as a basis for computing a μ controller.

In an attempt to satisfy both robust stability and robust performance with original specifications, a μ controller is computed based on D–K iterations. The resulting μ controller is reduced from 18 to 13 states by high-frequency residualized truncation and Hankel optimal norms. The nominal performance of the μ controller compares well with the nominal performance of the baseline H_∞ controller as illustrated in figures 4(a)–4(e). Note the lack of the superimposed second-order response on the altitude variable for the μ controller. However, in the robust performance, the advantage of a μ controller becomes apparent.

The frequency domain analysis indicates that the performance requirements are satisfied in the presence of 20-percent control effector uncertainty, so that the robust performance condition in figure 7 is met. The velocity, altitude, and angle-of-attack time histories are essentially the same for nominal and perturbed systems, as illustrated in figures 8(a)–8(c). The noticeable deviation of the perturbed response from the nominal value occurs for the variables that contain uncertainty. The time histories of the control variables exhibit differences that are due to the positive or negative value of the uncertainty because the controller tries to compensate for the uncertainty in effectiveness while attempting to achieve the desired response. The elevon response in figure 8(d) shows a small variation in the magnitude of the initial deflection; a smaller than nominal deflection for a 20-percent increase in effectiveness; and, conversely, a larger deflection for a 20-percent deterioration of effectiveness. The fuel flow rate in figure 8(e), shows that the difference between nominal and perturbed responses is more pronounced, although smoothness still characterizes each response.

In fact, the robust performance margin suggests that the system could withstand higher levels of control effector uncertainty and still fulfill performance requirements. The frequency analysis shown in figure 9 indicates that robust performance can be sustained for a closed-loop system with a 32.5-percent control effector uncertainty. The Δ used in the time simulations is a worst case, real-rational, stable perturbation with $\|\Delta_p\|_\infty = 1.0$. The closed-loop system time response is provided in figures 10(a)–10(e) for the nominal system and the ±32.5-percent uncertainty in control effectiveness. A comparison of nominal and worst case perturbed time responses shows that the μ controller successfully handles actuator uncertainty without sacrificing performance in most system variables. Some visible performance degradation occurs in the variables directly affected by the uncertainty, elevon, and fuel flow rate, but this degradation is not surprising. Despite some performance degradation compared with the ideal system response, all requirements on every system variable are satisfied, even with higher uncertainty than the 20 percent prescribed in the design. The encouraging preliminary results of the μ controller establish the technique as potentially successful in dealing with unique characteristics of hypersonic vehicles.

Conclusions

The applicability of robust control techniques to a single-stage-to-orbit air-breathing vehicle at hypersonic speeds on an ascent accelerating path and the effectiveness of these techniques are explored in this paper. Uncertainty is an integral part of hypersonic vehicle characteristics, so its effect on the analysis and synthesis of various control system design techniques is important to understand.

Several important issues related to control system design should be noted. The characteristics of air-breathing hypersonic vehicles and the requirements imposed on the control system translate explicitly into H_∞ domain specifications. Atmospheric turbulence has a noteworthy effect on the design of the H_∞ controller. The best performance should be exhibited by the controller designed for a nominal system (i.e., the assumption is that the physical system is perfectly represented by the model). However, the very fact that the system is apparently perfectly known makes the elevon sensitive enough to atmospheric turbulence to induce residual second-order behavior in the altitude response that it directly controls. In addition, this nominal H_∞ controller does not remain stable at 20-percent uncertainty, which is the prescribed level for this design problem.

The H_∞ controller, designed explicitly for 20-percent uncertainty, failed to provide the desired level of nominal system performance. The μ controller, designed for the same level of uncertainty, preserved the required performance and tolerated more than 50 percent more uncertainty than the design specified, thereby providing robust performance. This initial application indicates that the nature of uncertainty and how it is handled by the control design methodology have significant effects on the achievable level of system performance as well as on the tolerable level of system uncertainty.

Frequency-based linear analysis techniques imply the importance of μ as both the analysis and the synthesis tool for an air-breathing hypersonic vehicle. Even though the control laws were not tested in a full six-degree-of-freedom nonlinear simulation, the results are promising after the initial application of the structured singular value theory to an air-breathing hypersonic vehicle. The relatively fast design time is conducive to the tradeoff study between the achievable level of performance and the prescribed level of uncertainty. Such a study is valuable for the conceptual design as well as for the actual vehicle because the known physical parameter variations are explicitly considered and their relationships to the physical system are preserved. A timely tradeoff study can determine how much of the true physical uncertainty needs to be directly represented in the controller design to achieve the desired level of performance for the prescribed level of uncertainty.

Furthermore, because uncertainty occurs simultaneously from many different sources and the degree of uncertainty is high, the physical characteristics of the air-breathing hypersonic vehicle introduce structure into the problem. A methodology that takes full advantage of these physical characteristics is essential. The μ-analysis and synthesis technique preserves the structural relationship between uncertainty and performance variables, allowing the designer a systematic approach to explore tradeoffs between the two. Failure to account for this structural relationship can result in excessively conservative specifications and poor designs for an air-breathing hypersonic vehicle. Although further study is necessary before the structured singular value technique can be recommended as the method of choice for air-breathing hypersonic vehicles, the beginning research has been promising.

NASA Langley Research Center
Hampton, VA 23681-0001
April 1, 1994

Table I. Nominal Flight Conditions and Trim Accelerations

Mach	8.0
Dynamic pressure, psf	2005.8
Weight, lb	261 125.9
Moment of inertia, I_{yy}, slug-ft^2	9202.797
Center of gravity, x_{cg}, ft	10.0773
$\dot{V}$, ft/sec^2	30.6172
$\dot{\alpha}$, deg/sec	-1.4309×10^{-3}
$\dot{q}$, deg/sec^2	5.3973×10^{-4}
$\dot{\theta}$, deg/sec	1.634×10^{-2}
$\dot{h}$, ft/sec	163.146
V, ft/sec	7851.6
α, deg	2.1628
q, deg/sec	3.7754×10^{-2}
θ, deg	3.3534
h, ft	85 745.7
Elevon δe_o, deg	−9.0720
Throttle setting, η_o	1.2743
Fuel flow rate, lbm/sec	171.45

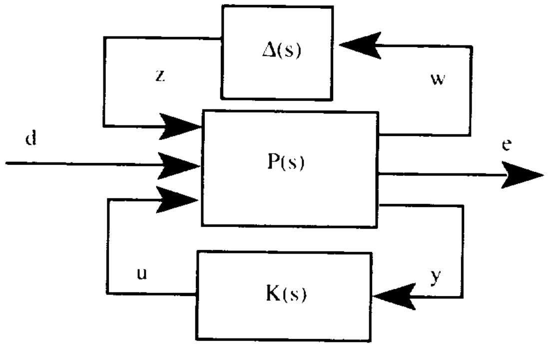

(a) General structure.

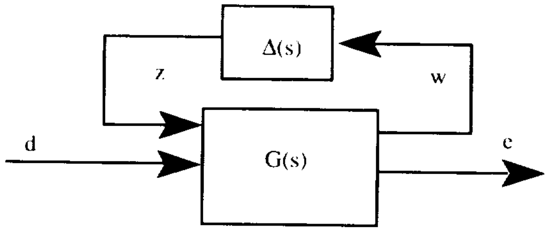

(b) Analysis structure.

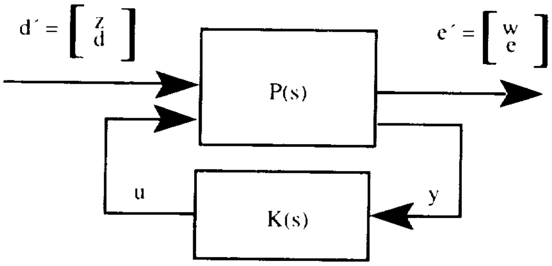

(c) Synthesis structure.

Figure 1. General framework used in robust feedback control system design. Any linear combination of inputs, outputs, and commands along with perturbations and controller can be viewed in context and rearranged to match appropriate diagram.

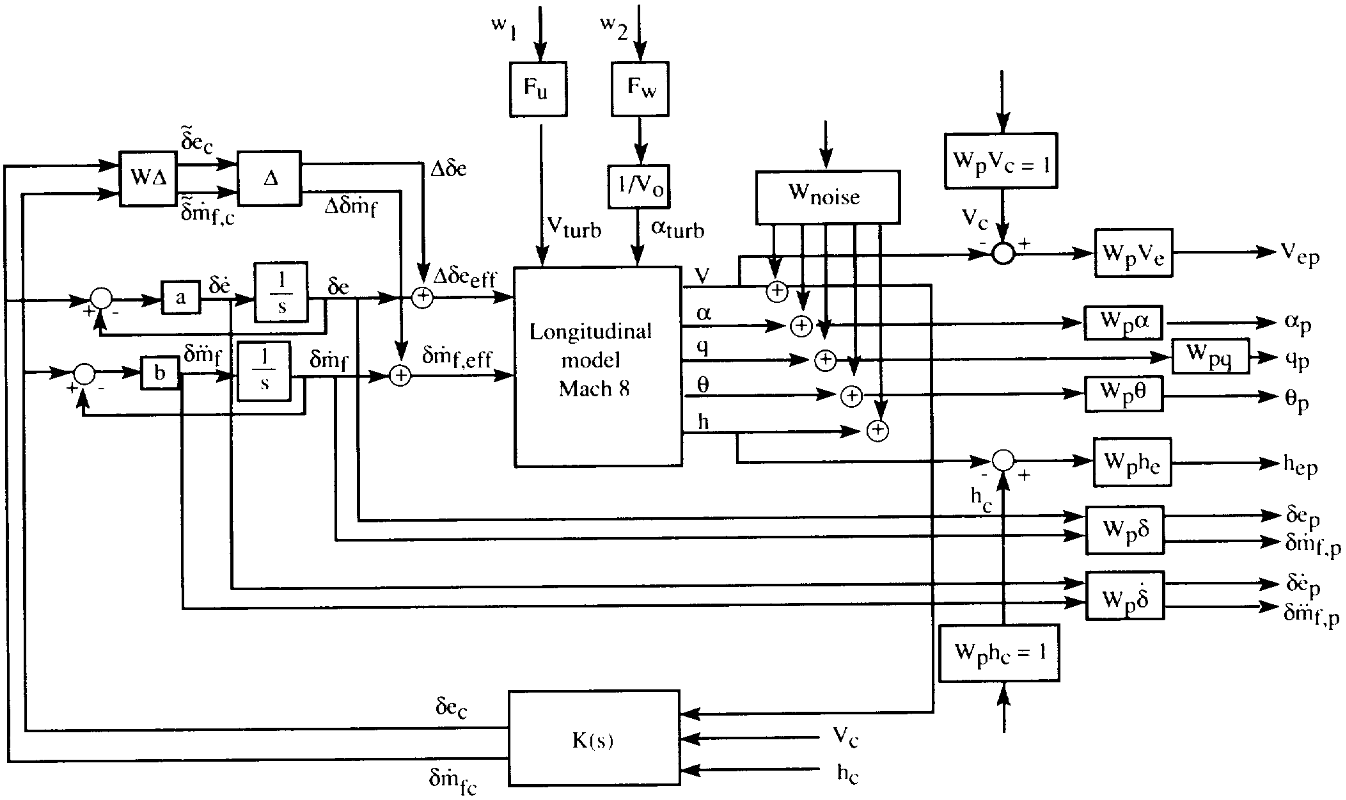

(a) Block diagram of interconnection structure for controller design.

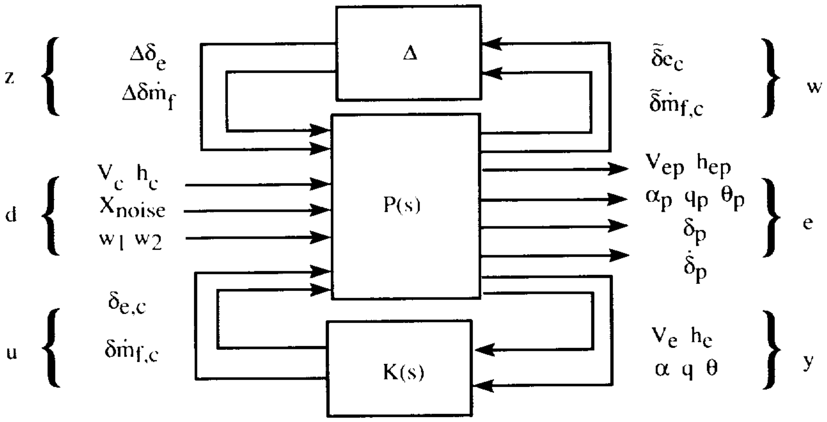

(b) Physical description of unity-bounded input and output sets of P.

Figure 2. Conical accelerator example problem formulation.

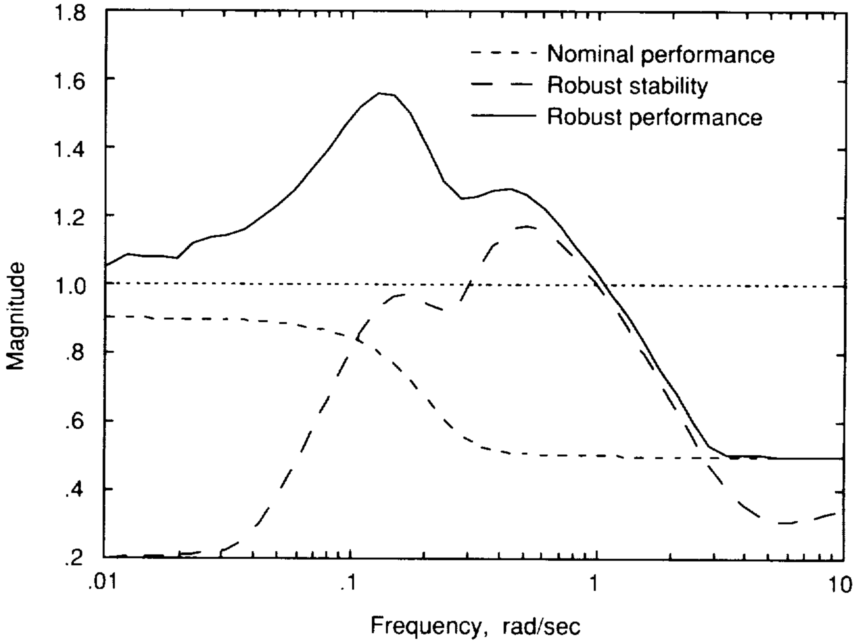

Figure 3. Frequency analysis of closed-loop system with H_∞ controller perturbed by 20-percent uncertainty in control effectiveness of both elevon and fuel flow rate.

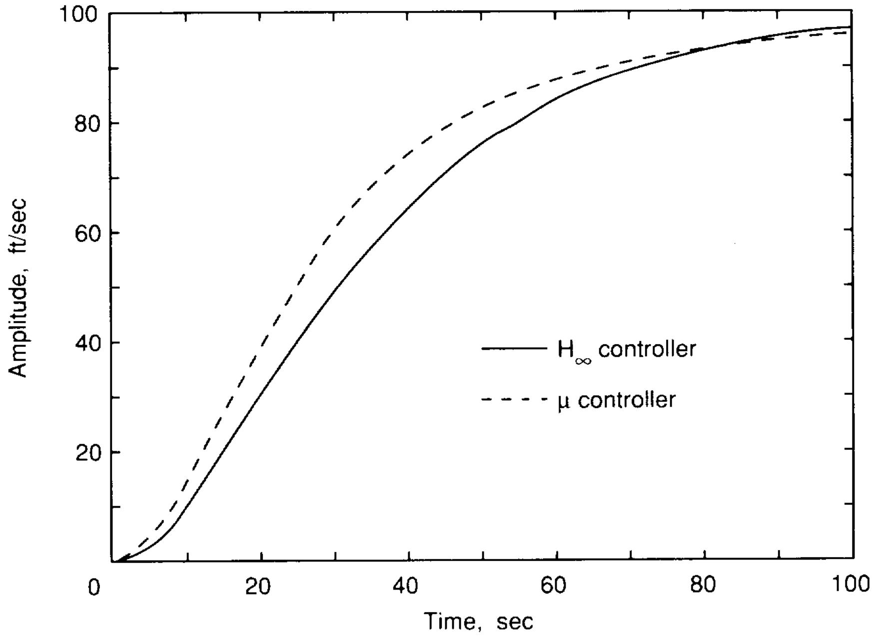

(a) Velocity.

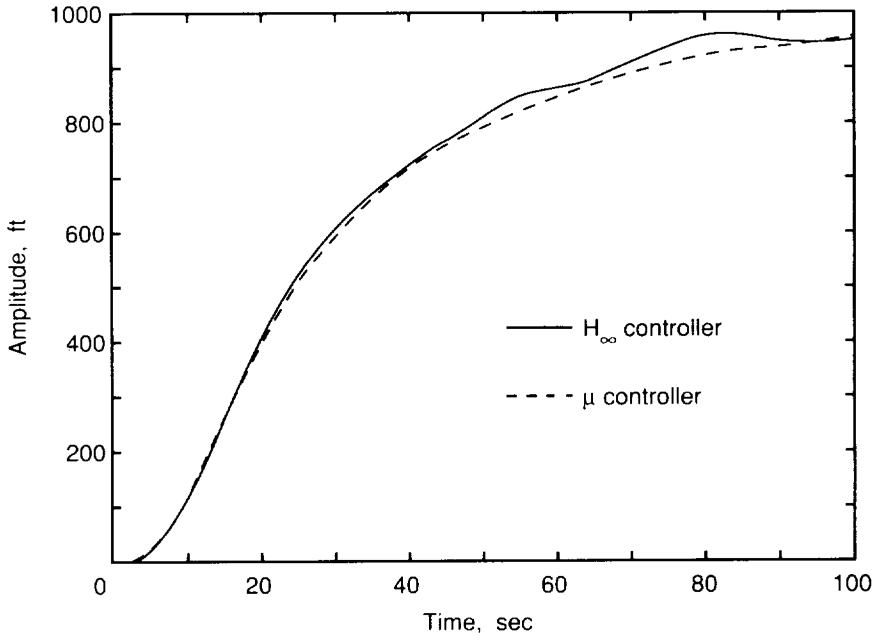

(b) Altitude.

Figure 4. Time response of nominal closed-loop system commanded to simultaneous 100 ft/sec velocity and 1000-ft altitude change while subjected to vertical and longitudinal atmospheric turbulence.

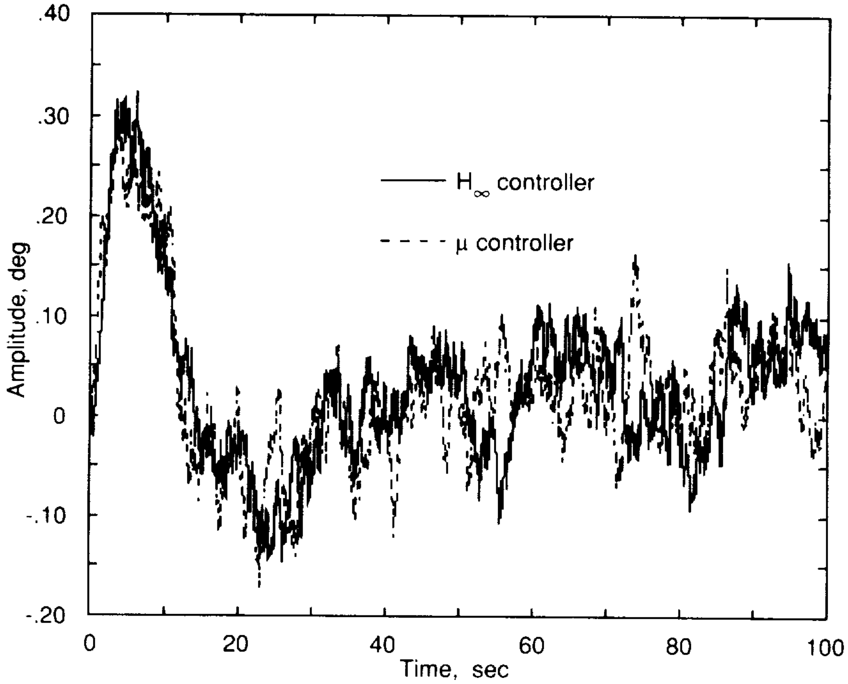

(c) Angle of attack.

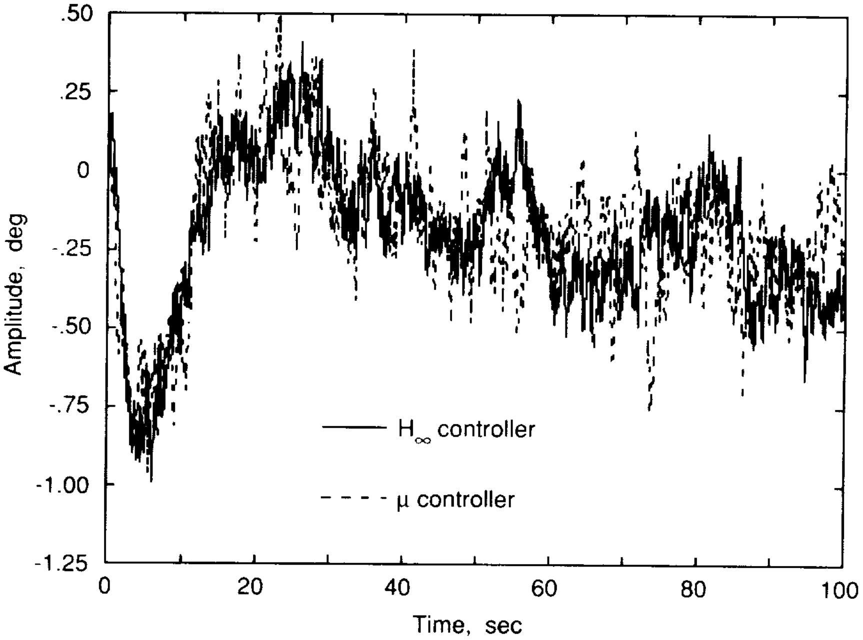

(d) Elevon.

Figure 4. Continued.

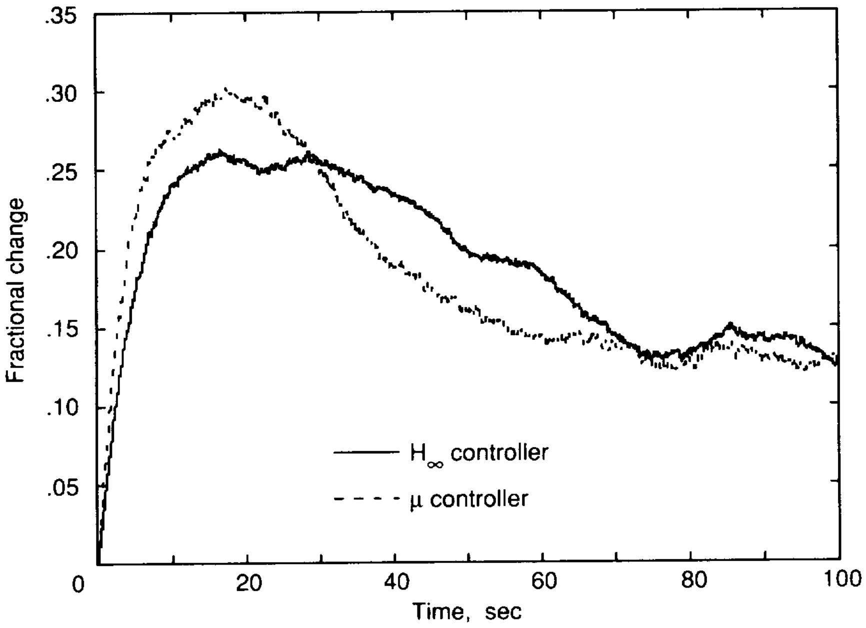

(e) Fuel flow rate.

Figure 4. Concluded.

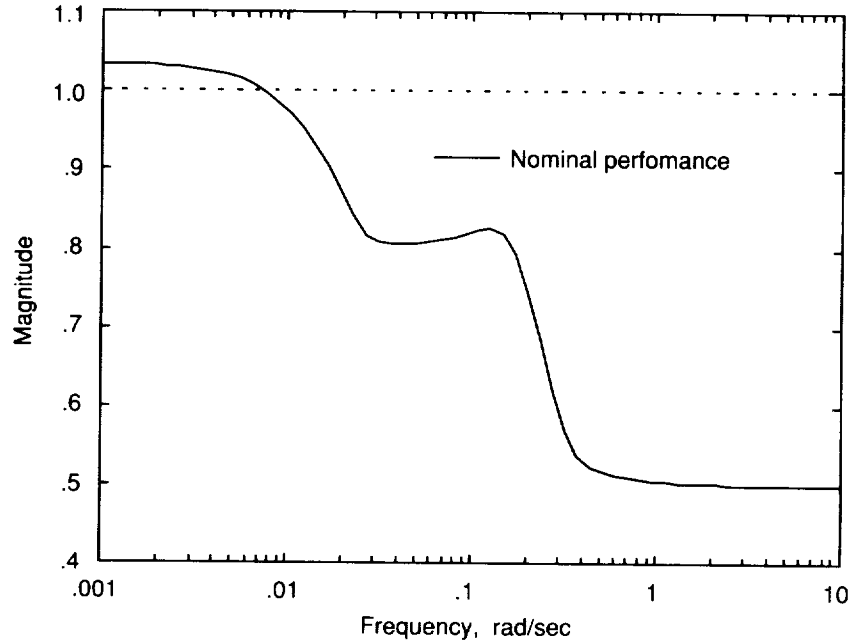

Figure 5. Nominal performance frequency analysis of closed-loop system with H_∞ controller designed for 20-percent uncertainty in control effectiveness of both elevon and fuel flow rate.

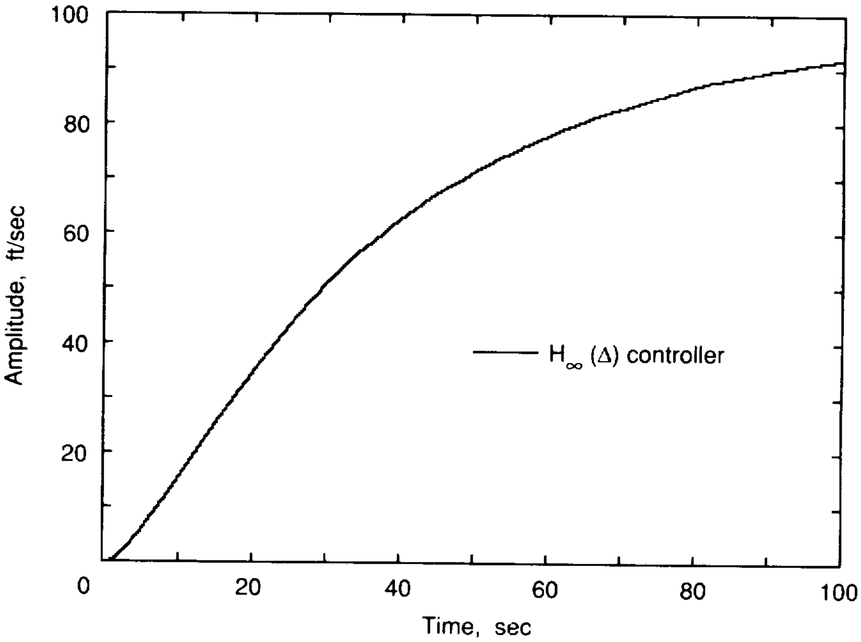

Figure 6. Velocity response to velocity command, altitude command, and vertical and longitudinal turbulence of system with H_∞ controller designed explicitly with 20-percent uncertainty in control effectiveness of both elevon and fuel flow rate.

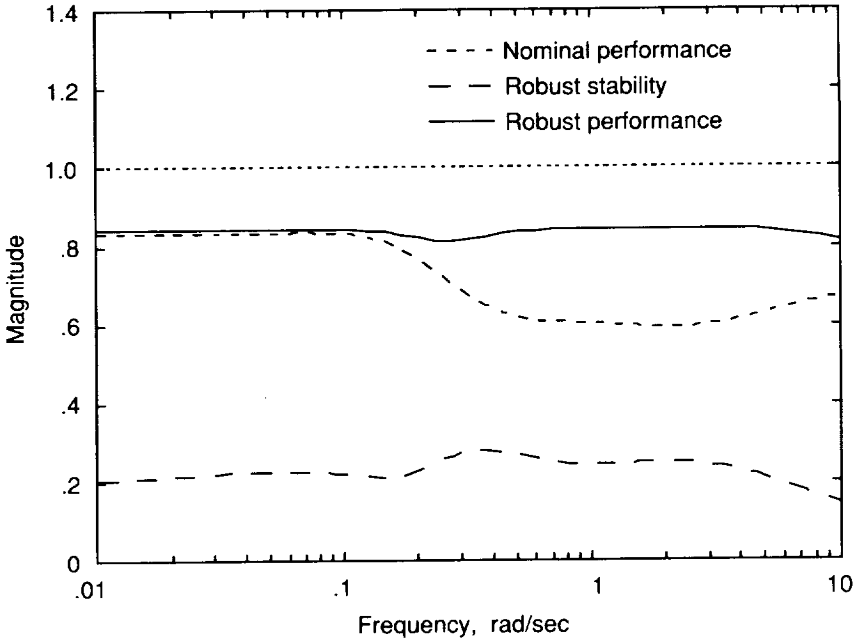

Figure 7. Frequency analysis of closed-loop system with μ controller perturbed by 20-percent uncertainty in control effectiveness of both elevon and fuel flow rate.

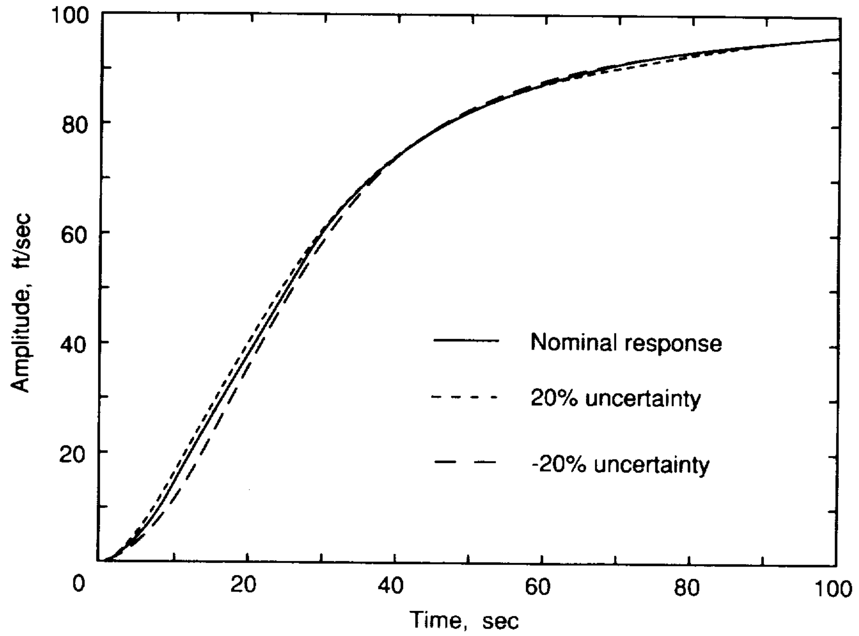

(a) Velocity.

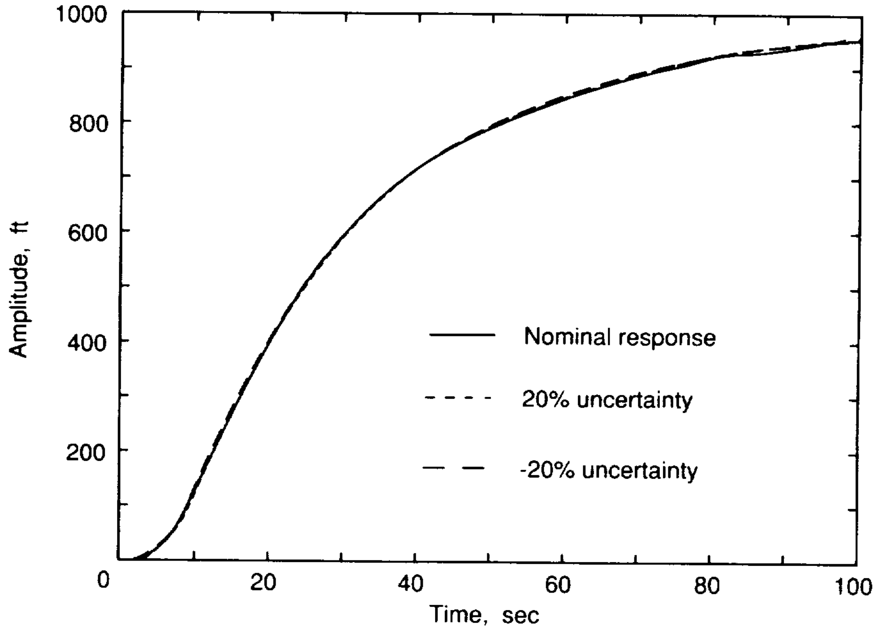

(b) Altitude.

Figure 8. Time history of nominal and perturbed (±20-percent uncertainty in effectiveness of elevon and fuel flow rate) closed-loop system with μ controller commanded to simultaneously increase velocity by 100 ft/sec and altitude by 1000 ft while subjected to vertical and longitudinal atmospheric turbulence.

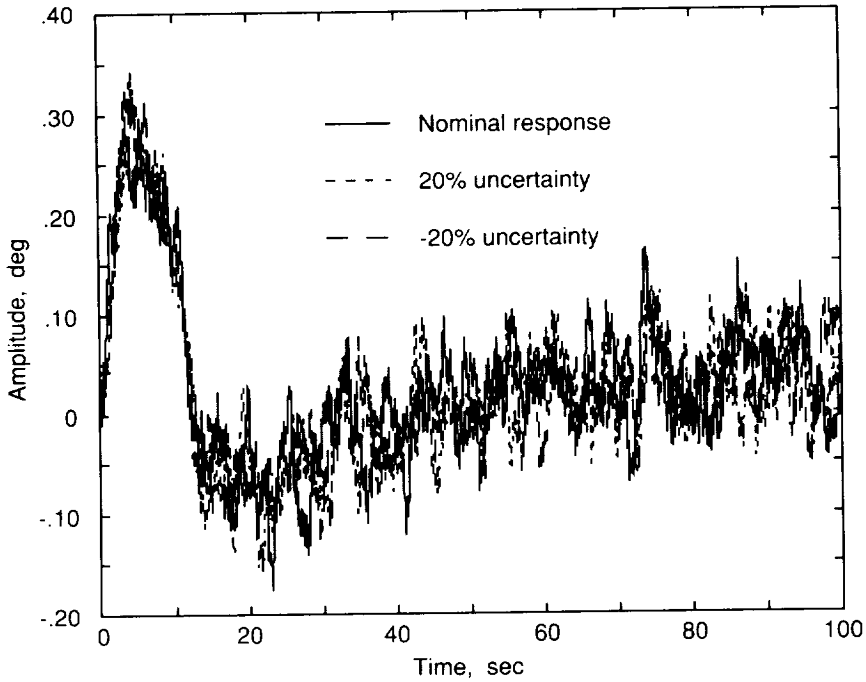

(c) Angle of attack.

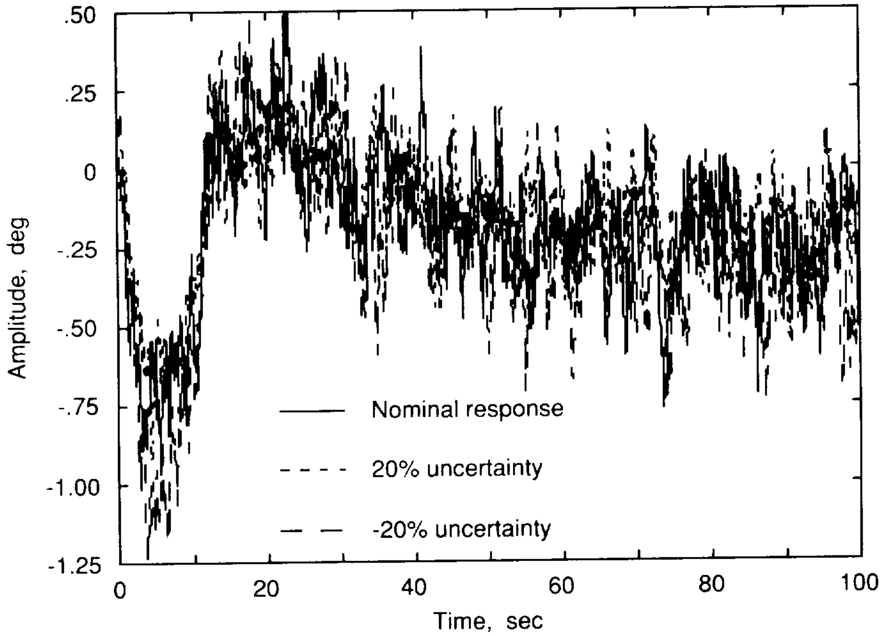

(d) Elevon.

Figure 8. Continued.

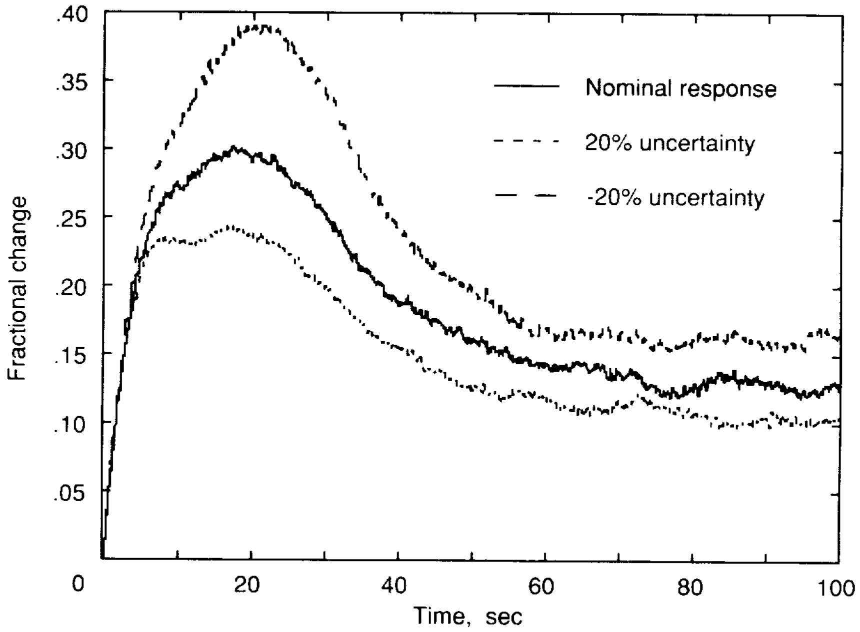

(e) Fuel flow rate.

Figure 8. Concluded.

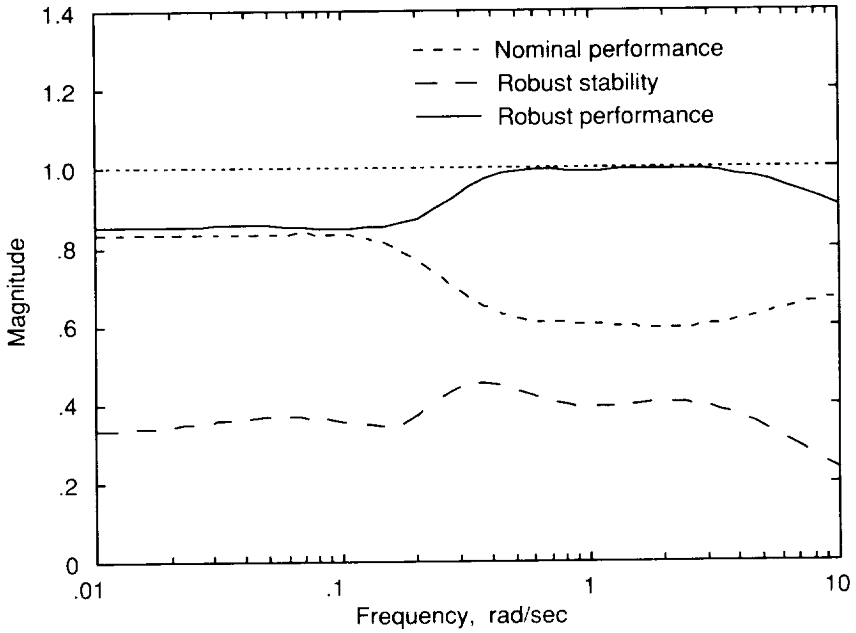

Figure 9. Frequency analysis of closed-loop system with μ controller perturbed by 32.5-percent uncertainty in control effectiveness of both elevon and fuel flow rate.

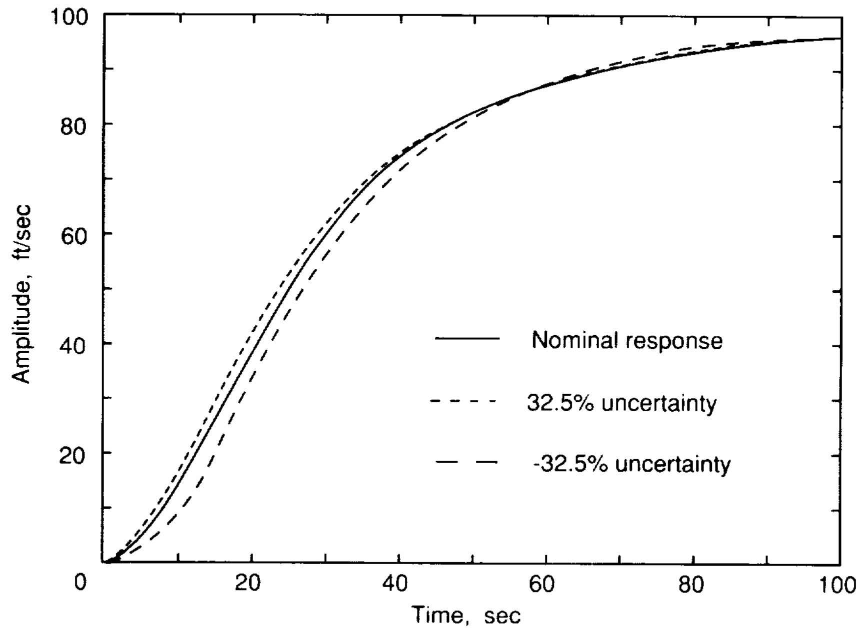

(a) Velocity.

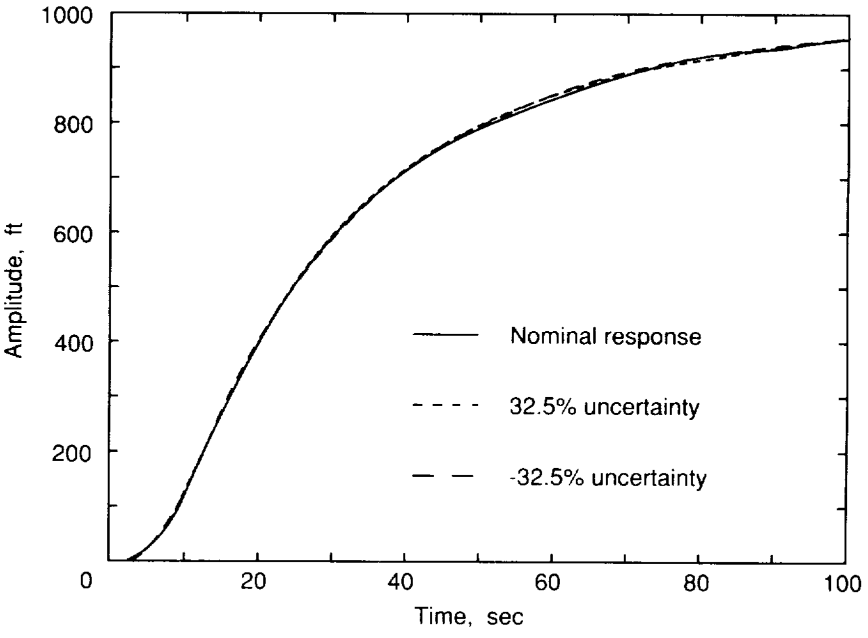

(b) Altitude.

Figure 10. Time history of nominal and perturbed (±32.5-percent uncertainty in effectiveness of elevon and fuel flow rate) closed-loop system with μ controller commanded to simultaneously increase velocity by 100 ft/sec and altitude by 1000 ft while subjected to vertical and longitudinal atmospheric turbulence.

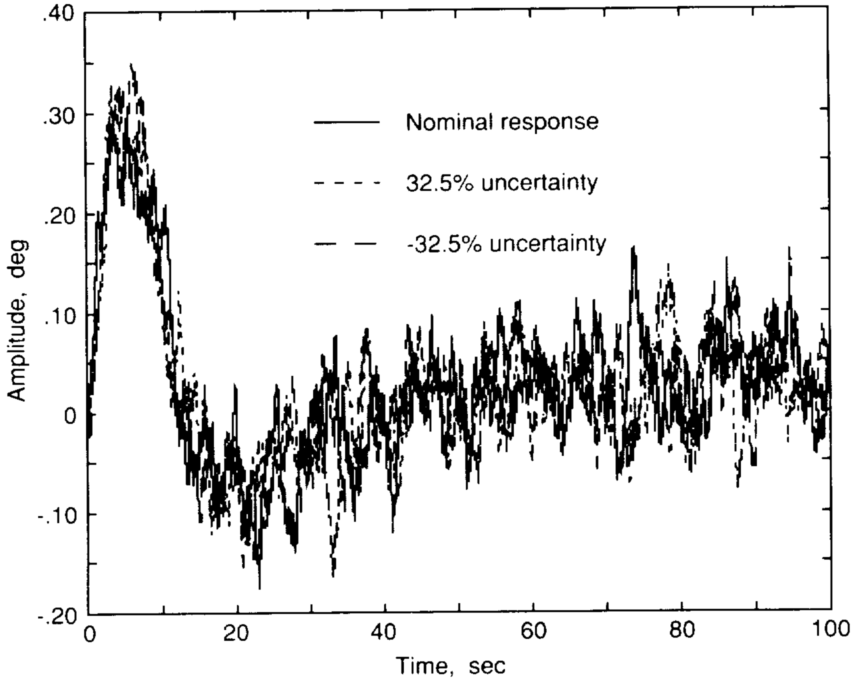

(c) Angle of attack.

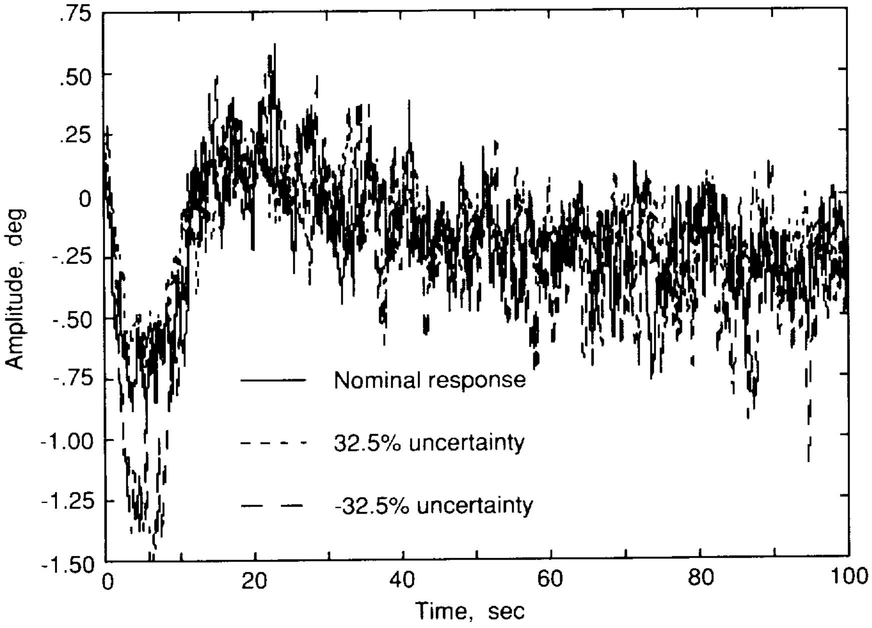

(d) Elevon.

Figure 10. Continued.

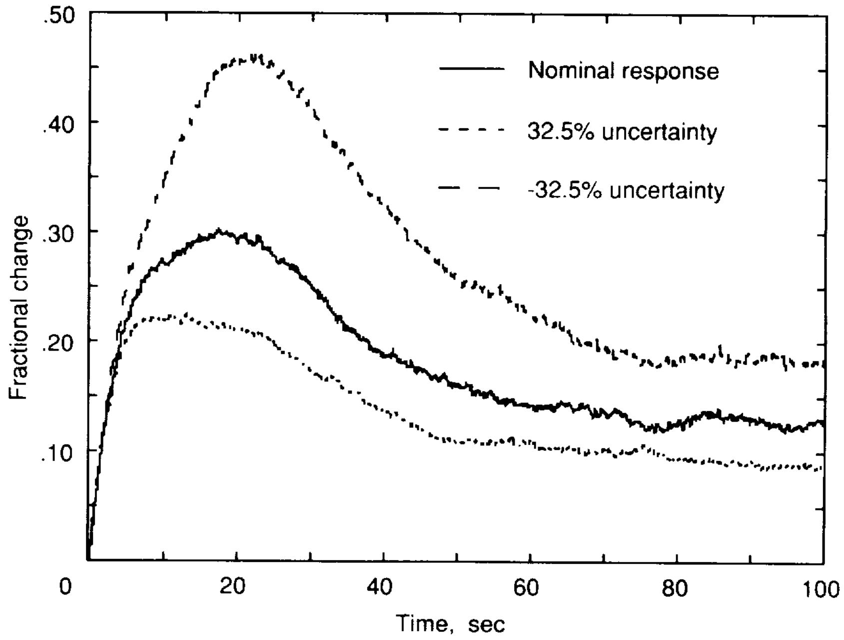

(e) Fuel flow rate.

Figure 10. Concluded.

Appendix A

Upgraded Propulsion Model for Conical Accelerator

The upgraded propulsion model for a conical accelerator presented in this appendix replaces the one given in reference 14. It was generated to eliminate certain inconsistencies in the original database and to provide a gridded, smooth propulsion model suitable for trajectory simulation, analysis, and optimization. The propulsion model in reference 14 had inconsistent characteristics in estimating propulsion system performance at values of η away from unity. These inconsistencies occurred because the propulsion modeling codes were run at relatively few analysis points (about $\eta = 1$ for different Mach numbers) and the database was then padded with extrapolated values to extend the range. However, the extrapolated data points violated a fundamental relationship between thrust coefficient (C_T, ft^2 thrust per dynamic pressure) and specific impulse.

The upgraded model makes use of the data at certain calculated points that were theoretically predicted (ref. 14) and approximates the generic performance of this class of propulsion systems at grid points where the data are unavailable. At a given Mach number, C_T was assumed to have a nearly linear variation with η for values of η exceeding unity. Moreover, C_T was assumed to rapidly decrease as η was decreased below 0.3 to simulate an engine unstart. A general curve-fitting algorithm was employed to fit C_T data at certain calculated points while maintaining the aforementioned trends. The curve fit was then used to extract C_T at a prespecified set of η values. To obtain the specific impulse ($I_{\rm sp}$, sec) at this set of η values, the following relationship was used:

$$I_{\rm sp}(\eta, M_1) = \frac{C_T(\eta, M_1) I_{\rm sp}(\eta_1, M_1)\eta_1}{C_T(\eta_1, M_1)} \tag{A1}$$

for a specified M_1 and η_1. Equation (A1) can be derived using the definition of $I_{\rm sp}$ and η and the assumption that the air mass flow through the engines is a constant at a given Mach number. Thus,

$$\eta = \frac{\dot{m}_f}{0.029\,\dot{m}_a} \tag{A2}$$

$$I_{\rm sp} = \frac{\bar{q} C_T}{\dot{m}_f g} \tag{A3}$$

In the above equations, $\bar{q}$ and g are dynamic pressure and acceleration due to gravity, respectively. The above procedure was repeated at all Mach numbers to generate a grid. Furthermore, the upgraded propulsion model is simplified by eliminating the variation of C_T and $I_{\rm sp}$ with $\bar{q}$ and by taking into account the weak dependence, especially in the lower Mach number range ($M < 15$).

The upgraded model consists of two sets of tables: one set for the low-speed propulsion cycle (Mach = 0.3 to 2) and another set for the high-speed propulsion cycle (Mach = 2 to 25). The C_T and $I_{\rm sp}$ values are given in tables AI and AII for the low-speed propulsion cycle and in tables AIII and AIV for the high-speed propulsion cycle. Axial thrust T (lb) and fuel flow rate $\dot{W}$(lb/sec) are computed as follows:

$$T = \bar{q} C_T(M, \eta) \tag{A4}$$

$$\dot{W} = \frac{T}{I_{\rm sp}(M, \eta)} \tag{A5}$$

Note that the propulsion model is not continuous at a Mach number of 2, which would represent discrete switching from low- to high-speed cycles. To avoid this discontinuity, the data could be linearly interpolated between a Mach number of 1.5 (low-speed cycle) and a Mach number of 2.0 (high-speed cycle) to simulate a gradual transition from the low- to the high-speed propulsion cycle.

Table AI. Low-Speed Thrust Coefficent as Function of Mach Number and Fuel Equivalence Ratio

η	Low-speed thrust coefficient for Mach number of						
	0.3	0.5	0.7	0.9	1.0	1.5	2.0
0.5	1047.6	503.61	364.83	294.02	273.68	198.56	163.28
.6	1257.0	595.11	425.86	341.86	318.28	233.55	194.01
.7	1466.5	683.53	482.91	386.03	359.50	266.97	224.09
.8	1675.9	768.88	535.98	426.54	397.34	298.82	253.54
.9	1885.3	851.15	585.08	463.39	431.81	329.10	282.34
1.0	2094.7	930.35	630.19	496.58	462.89	357.81	310.50
1.1	2301.0	1006.5	671.32	526.11	490.59	384.94	338.02
1.2	2513.3	1079.5	708.48	551.98	514.92	410.50	364.89
1.3	2722.6	1149.5	741.65	574.19	535.87	434.49	391.12
1.4	2931.9	1216.4	770.85	592.75	553.44	456.91	416.72
1.5	3141.2	1280.2	796.06	607.64	567.63	477.75	441.66
1.6	3350.5	1341.0	817.30	618.88	578.44	497.02	465.97
1.7	3559.7	1398.6	834.56	626.45	585.87	514.72	489.63
1.8	3768.9	1453.2	847.84	630.37	589.92	530.85	512.65
1.9	3978.1	1504.7	857.14	630.63	590.58	545.40	535.03
2.0	4187.2	1553.2	862.46	627.23	587.89	558.38	556.77

Table AII. Low-Speed Specific Impulse as Function of Mach Number and Fuel Equivalence Ratio

η	Low-speed specific impulse for Mach number of						
	0.3	0.5	0.7	0.9	1.0	1.5	2.0
0.5	1894.0	2332.2	2896.3	3254.9	3299.5	2860.4	2512.6
.6	1893.9	2296.6	2817.3	3153.7	3197.7	2803.8	2487.8
.7	1893.8	2261.0	2738.3	3052.4	3095.8	2747.2	2463.1
.8	1893.7	2225.4	2659.4	2951.1	2994.0	2690.6	2438.4
.9	1893.6	2189.8	2580.4	2849.9	2892.2	2633.9	2413.7
1.0	1893.5	2154.2	2501.4	2748.6	2790.3	2577.3	2389.0
1.1	1893.4	2118.6	2422.5	2647.3	2688.5	2520.7	2364.3
1.2	1893.4	2083.0	2343.5	2546.0	2586.6	2464.0	2339.6
1.3	1893.3	2047.4	2264.5	2444.8	2484.8	2407.4	2314.9
1.4	1893.2	2011.8	2185.5	2343.5	2383.0	2350.8	2290.2
1.5	1893.1	1976.2	2106.6	2242.2	2281.1	2294.2	2265.4
1.6	1893.0	1940.6	2027.6	2141.0	2179.3	2237.5	2240.7
1.7	1892.9	1905.0	1948.6	2039.7	2077.4	2180.9	2216.0
1.8	1892.8	1869.4	1869.6	1938.4	1975.6	2124.3	2191.3
1.9	1892.7	1833.8	1790.7	1837.1	1873.7	2067.7	2166.6
2.0	1892.6	1798.2	1711.7	1735.9	1771.9	2011.0	2141.9

Table AIII. High-Speed Thrust Coefficent as Function of Mach Number and Fuel Equivalence Ratio

η	High-speed thrust coefficient for Mach number of								
	2	3	4	6	8	10	15	20	25
0.25	205.04	147.41	97.613	5.631	65.041	49.924	28.204	24.548	12.904
.50	315.57	236.30	181.66	109.21	113.27	83.254	50.136	44.460	24.635
.75	391.29	303.64	252.14	160.75	140.52	102.74	64.496	58.078	33.843
1.0	451.44	361.34	309.05	210.23	156.16	115.38	74.624	68.082	41.566
1.5	553.90	465.68	409.85	307.23	171.55	130.85	88.167	82.205	54.488
2.0	651.48	566.99	510.65	404.23	180.42	140.50	97.357	92.411	65.602
2.5	753.04	670.76	611.45	501.23	189.71	147.95	104.77	100.97	75.82
3.0	861.74	778.94	712.25	598.23	200.98	154.73	111.59	108.96	85.59
4.0	1104.1	1010.7	913.84	792.23	225.90	168.77	125.64	125.28	104.68
5.0	1379.6	1263.1	1115.4	986.23	242.09	184.95	141.73	143.51	123.85

Table AIV. High-Speed Specific Impulse as Function of Mach Number and Fuel Equivalence Ratio

η	High-speed specific impulse for Mach number of								
	2	3	4	6	8	10	15	20	25
0.25	5672.4	5054.6	3877.4	2891.8	3760.2	3214.1	1948.7	1885.1	1096.5
.50	4365.0	4051.3	3607.9	2838.5	3274.3	2679.9	1732.1	1707.0	1046.7
.75	3608.3	3470.6	3338.5	2785.3	2708.0	2204.6	1485.4	1486.6	958.60
1.0	3122.2	3097.5	3069.0	2732.0	2257.0	1857.0	1289.0	1307.0	883.00
1.5	2553.9	2661.3	2713.3	2661.7	1652.9	1404.0	1015.3	1052.1	771.68
2.0	2252.9	2430.2	2535.5	2626.5	1303.8	1130.6	840.85	887.02	696.81
2.5	2083.2	2300.0	2428.8	2605.5	1096.8	952.45	723.89	775.34	644.28
3.0	1986.6	2225.8	2357.6	2591.4	968.24	830.11	642.53	697.28	606.11
4.0	1909.0	2166.1	2268.7	2573.8	816.24	679.04	542.54	601.27	555.95
5.0	1908.3	2165.5	2215.4	2563.3	699.78	595.35	489.64	551.01	526.19

Appendix B

Linear Model Development From Nonlinear Simulation

This appendix describes the conceptual development of the linear models of a conical accelerator vehicle. The linear models were derived numerically from the 6-DOF nonlinear rigid-body simulation of the vehicle using the program to optimize simulated trajectories (POST). (See ref. 18.) The POST simulation is for a general, rigid-body, 6-DOF trajectory with discrete parameter trajectory targeting and optimization. The 6-DOF simulation of the vehicle is built by specifying the vehicle aerodynamics, propulsion, and mass properties and the environment in which the vehicle operates. For the 6-DOF rigid-body simulation of a conical accelerator, the aerodynamics and mass properties in reference 14 were used along with the propulsion model given in appendix A. To derive the linear models, a spherical nonrotating planet model with a stationary atmosphere (a 76 U.S. Standard Atmosphere option chosen in POST) was assumed to define the operating environment. Linear models of the vehicle dynamics at the desired flight conditions were extracted using the targeting feature of the POST simulation.

The targeting option in the POST simulation allows a user to solve a nonlinear programming problem wherein a user-defined set of dependent variables (constraints) must be driven to their desired values by changing a set of user-defined independent variables (controls). The solution of the nonlinear programming problem is obtained from a gradient-based optimization algorithm. A special case of the targeting problem is the trim problem wherein a set of dependent variables, usually vehicle accelerations at a given instance are required to take on some user-specified set of desired values by allowing the program to change a set of independent variables (i.e., control effectors). The trim problem and the fact that the solution of this problem is obtained by a gradient-based algorithm are exploited to numerically derive the linear models at a given flight condition.

To get the linear models, a special trim problem is posed in the POST simulation. In this case, the dependent variables are defined to be vehicle translational and rotational accelerations; the independent variables are vehicle states and control effectors. To solve this problem, the POST simulation calculates the numerical partial derivative of each of the dependent variables with respect to each independent variable by using a forward differencing scheme. The Jacobian, which consists of the first-order terms of the Taylor series expansion of the nonlinear equations of motion about the analysis point (the chosen flight conditions), is extracted and partitioned appropriately to give the linear system state space representation. Note that the analysis point is completely arbitrary; that is, the analysis point could be a nonequilibrium flight condition wherein vehicle accelerations are nonzero or it could be a steady-state flight condition. However, nonlinear equations of motion linearized at nonequilibrium flight conditions result in linear systems that are time varying and special care must be exercised while using them in conjunction with LTI design and analysis procedures.

Appendix C

Weighting Function Derivation

The performance weighting function W_p enters into the control law design through the following relationship:

$$\|G(j\omega)W_p(j\omega)\|_\infty = 1 \qquad \text{(C1)}$$

where $G(j\omega)$ is any transfer function between the input and output of interest. From classical control, it is known, for example, that if a small steady-state error is desired, then the transfer function between the error and reference signal should be small in the frequency range of interest. The same is true for any set of input/output combinations. Thus, if $G(j\omega)$ must be small at low frequencies for good tracking performance, then, conversely, W_p must be large. In addition, from the Bode integral theorem, $G(j\omega)$ must become large at high frequencies, thus forcing W_p to become small. Based on the criterion described in equation (C1) and on the relationships derived from classical control, the method presented in this section can be used to calculate W_p.

Combining specifications of steady-state error, percentage of overshoot, and time constant for the variable of interest, the time domain specifications can be directly translated into a frequency-dependent transfer function in the H_∞ domain. Common relationships from classical control make the time constant τ of the response equivalent to the inverse of the crossover frequency for the descriptive transfer function. Furthermore, applying the final value theorem yields the steady-state tracking error that is analogous to the inverse of low-frequency system gain. The performance weighting function is for a high-pass filter, so low-frequency gain can be also interpreted as the amount by which disturbances are attenuated. Thus, a performance weighting function construction proceeds as follows. Assume the transfer function has the form

$$W_p(j\omega) = K\frac{a\ j\omega + 1}{b\ j\omega + 1} \qquad \text{(C2)}$$

Because low-frequency gain gives a steady-state error, let

$$\omega \rightarrow 0 : K_{\text{lf}} = K = \frac{1}{e_{ss}} \qquad \text{(C3)}$$

From the Bode diagram at crossover frequency ω_c,

$$L_m|W_p(j\omega_c)| = 0 \text{ implies that } |W_p(j\omega_c)| = 1$$

Solving for ω_c results in

$$\omega_c = \frac{1}{\tau} = \sqrt{\frac{1 - K^2}{K^2a^2 - b^2}} \qquad \text{(C4)}$$

The desired percentage of overshoot is related to high-frequency gain, but the relationship is not obvious. The relationship deduced here is based on the damping ratio and peak magnitude of the Bode plot. Because the damping ratio ζ is related to overshoot by

$$\text{Percent overshoot} = e^{-\zeta\pi/\sqrt{1-\zeta^2}}$$

the peak magnitude of the standard second-order transfer function for the desired overshoot can be obtained from the Bode plot. As the values of ζ approach critical damping (0.707), the peak magnitude approaches 0 dB and this method no longer applies. However, for $\zeta < 0.707$, the inverse of peak magnitude serves as the high-frequency gain K_{hf}, resulting in

$$\omega \rightarrow \infty : K_{\text{hf}} = \frac{Ka}{b} \qquad \text{(C5)}$$

Hence, equations (C3)–(C5) can be solved for the three unknowns K, a, and b. Equation (C3) gives the value for K. The expression for b from equation (C5) is substituted into equation (C4) and the resulting equation is solved for a, yielding

$$a^2 = \frac{b^2\omega_c^2 - 1 + K^2}{K^2\omega_c^2}$$

Thus,

$$a = \sqrt{\frac{K^2 - 1}{K^2\omega_c^2 - \frac{K^2\omega_c^2}{K_{\text{hf}}^2}}} \qquad \text{(C6)}$$

For example, to calculate the performance transfer function for velocity response to velocity command, let

$e_{ss} = 5\% = 0.05 \rightarrow K = 20$

$\tau = 40 \text{ sec} \rightarrow \omega_c = 0.025$

$10\% \text{ overshoot} \rightarrow \zeta = 0.6 \rightarrow K_{\text{hf}} = 0.97$

The resulting transfer function does not guarantee that the variable of interest will follow the specified performance. The three response specifications are not physically independent of each other so even if they are independently designated in the performance weighting, the desired response would not be attained without knowing the physical capabilities or inclinations of the variables. In the example problem, the achieved overshoot is a much more direct function of the specified time constant than of the specified overshoot in the commanded variables. Moreover, for the time constants specified in the problem, the commanded variables were unlikely to produce large overshoots even when allowed by the performance weightings (i.e., ζ was notably relaxed). In fact, the overshoot specification that was incorporated into W_p had to be relaxed because it considerably slowed the time constant. The overshoot incorporated into W_p that produced the actual specified response was 40 percent (40% overshoot $\rightarrow \zeta = 0.3 \rightarrow K_{\mathrm{hf}} = 0.5$). Similar adjustment had to performed on the steady-state error that was incorporated into W_p. The desired steady-state error was less than 5 percent; the one incorporated into W_p was 1 percent.

The time constant for velocity response, remained at 40 sec which resulted in

$$W_p V_c = \frac{0.5(s + 4.330 \times 10^{-2})}{s + 2.165 \times 10^{-4}} \qquad \text{(C7)}$$

The altitude response had a propensity for faster rise time than was specified. To minimize the elevon response that directly affected the angle of attack, the altitude time constant was increased to 45 sec, which resulted in the transfer function

$$W_{ph_c} = \frac{0.5(s + 3.849 \times 10^{-2})}{s + 1.925 \times 10^{-4}} \qquad \text{(C8)}$$

The weighting of α was based on the desire to attenuate atmospheric turbulence and to indicate the importance of α response in the optimization process. The starting number was 10 and the final constant was derived by iteration. However, as mentioned above, elevon response has a great deal more effect on α response than the actual α weighting. Unity weightings on q and θ indicated those responses are of secondary importance. Due to the linear relationship linking α, θ, and γ (flight path angle) that was assumed here, the magnitude of the θ response was similar to that of α. Moreover, q was also linked by a linear relation to θ. Consequently, both q and θ responses were satisfactory and resulted from the constant weightings

$$W_p \begin{bmatrix} \alpha \\ q \\ \theta \end{bmatrix} = \begin{bmatrix} 20 \\ 1 \\ 1 \end{bmatrix} \qquad \text{(C9)}$$

The actuator position and rate limits were imposed by

$$W_p \begin{bmatrix} \delta e \\ \delta \dot{m}_f \end{bmatrix} = \begin{bmatrix} 30 \\ 60 \end{bmatrix} \qquad \text{(C10)}$$

$$W_p \begin{bmatrix} \delta \dot{e} \\ \delta \ddot{m}_f \end{bmatrix} = \begin{bmatrix} 20 \\ 10 \end{bmatrix} \qquad \text{(C11)}$$

where the position weighting function started as an allowable deflection limit for the elevon (±20°) and for the fuel flow rate (60 percent). To minimize elevon deflection, the weighting function had to be increased. The actuator rate weightings were similarly established. The starting point was the assumed rate limit that had to be relaxed for both control variables to achieve satisfactory responses.

Appendix D

Numerical Systems

The longitudinal dynamics are represented by

$$\dot{x} = Ax + Bu \tag{D1}$$

where

$$x = \begin{bmatrix} V \\ \alpha \\ q \\ \theta \\ h \end{bmatrix}$$

$$u = \begin{bmatrix} \delta e \\ \eta \end{bmatrix}$$

The system and control matrices are set at a Mach number of 8, an altitude of 85 700 ft, and a dynamic pressure trajectory of 2000 psf to give

$$A = \begin{bmatrix} 3.65424 \times 10^{-3} & -9.6679 \times 10^{-1} & 0 & -5.5639 \times 10^{-1} & -1.4321 \times 10^{-3} \\ -3.91925 \times 10^{-5} & -8.1626 \times 10^{-2} & 1.0000 & -8.4420 \times 10^{-5} & 9.2560 \times 10^{-6} \\ 2.0147 \times 10^{-3} & 3.0354 & -9.5218 \times 10^{-2} & 1.5500 \times 10^{-5} & -1.0766 \times 10^{-5} \\ 2.7263 \times 10^{-6} & 7.7679 \times 10^{-6} & 1.0000 & -7.7679 \times 10^{-6} & -1.0188 \times 10^{-9} \\ 2.0779 \times 10^{-2} & -1.3701 \times 10^{2} & 0 & 1.3701 \times 10^{2} & 0 \end{bmatrix}$$

and

$$B = \begin{bmatrix} 9.6995 \times 10^{-2} & 7.5989 \\ 3.3486 \times 10^{-3} & -2.0942 \times 10^{-3} \\ 1.0825 & 0 \\ 0 & 0 \\ 0 & 0 \end{bmatrix}$$

Aerodynamic forces and moments on the airplane depend on the relative motion of the airplane in the atmosphere and not on the inertial velocities. To account for atmospheric disturbances, the forces and moments must be related to the relative motion with respect to the atmosphere. This accounting is done by expressing velocities used in calculating aerodynamics in terms of the inertial and gust velocity components. Hence, the atmospheric turbulence is introduced conventionally into the state equations as

$$\dot{x} = Ax + Bu + Ev \tag{D2}$$

where

$$E = \begin{bmatrix} -3.6524 \times 10^{-3} & 9.6679 \times 10^{-1} \\ 3.9195 \times 10^{-5} & 8.1626 \times 10^{-2} \\ -2.0147 \times 10^{-3} & -3.0354 \\ 0 & 0 \\ 0 & 0 \end{bmatrix}$$

$$v = \begin{bmatrix} V_{\text{gust}} \\ \alpha_{\text{gust}} \end{bmatrix}$$

Here, gust matrix terms $\dot{\theta}$ and $\dot{h} = 0$ because they depend strictly on inertial velocities.

The H_∞ controller is a dynamic suboptimal compensator with the number of states n that is equivalent to the number of generalized plant P states; for this problem, $n = 12$. The state equations representing the system are

$$
\begin{bmatrix} \dot{\xi}_1 \\ \vdots \\ \dot{\xi}_n \end{bmatrix} = A_c \begin{bmatrix} \xi_1 \\ \vdots \\ \xi_n \end{bmatrix} + B_c \begin{bmatrix} V \\ \alpha \\ q \\ \theta \\ h \\ V_c \\ h_c \end{bmatrix}
$$

$$
\begin{bmatrix} \delta e \\ \delta \dot{m}_f \end{bmatrix} = C_c \begin{bmatrix} \xi_1 \\ \vdots \\ \xi_n \end{bmatrix} \tag{D3}
$$

The μ controller is based on the H_∞ controller with the generalized plant P scaled by matrices D and D^{-1} to reflect the structure of the uncertainty and has the same state space form as shown in equation (D3). Thus, the new plant $\tilde{P} = DPD^{-1}$ is augmented by the states of D and D^{-1} during each iteration, with the final controller containing 18 states. The controller was reduced using the truncation with residue and optimal Hankel singular values methods. The resultant 13-state controller produced an essentially identical response in a closed-loop system as the original μ controller.

For completeness, the poles of the H_∞ controller are given in the table for the nominal system (referred to as the baseline controller), for an H_∞ controller that is designed for 20-percent uncertainty, and for a μ controller that is based on the latter H_∞ controller. Neither the H_∞ controllers nor the μ controller have transmission zeros. The closed-loop functions for the controllers are also characterized as having no transmission zeros.

The H_∞ baseline controller remains robustly stable to 17-percent uncertainty, so the destabilizing perturbation in a simulation must satisfy $\|W_\Delta \Delta_s\|_\infty = 0.17$. The peak value $\mu[G_{11}(j\omega)] = 1.174$ for 20-percent uncertainty implies that the system will remain stable for $\|\Delta\|_\infty = 1/1.174 = 0.85$ instead of for $\|\Delta\|_\infty = 1$. This value also implies that $\|W_\Delta \Delta_s\|_\infty = \|0.20 \cdot 0.85\|_\infty = 0.17$. The μ controller not only remains stable but also satisfies robust performance for 32.5-percent uncertainty (the robust performance criterion, $\mu[G(j\omega)] \rightarrow 1$, so the worst case performance perturbation must satisfy $\|W_\Delta \Delta_p\|_\infty = 0.325$ in a simulation.

Nominal System

Poles	Frequency	Damping
$K_{\chi}(\Delta = 0), n = 12$		
$-2.0407 \times 10^{-4} \pm j1.4148 \times 10^{-5}$	2.0456×10^{-4}	0.998
$-1.3431 \times 10^{-1} \pm j1.7063 \times 10^{-1}$	.21715	.619
-2.7473	-2.7473	1.0
$-2.5096 \pm j4.9674$	5.5654	.451
42.583	42.583	-1.0
$-65.745 \pm j68.746$	95.124	.691
$-293.56 \pm j275.83$	402.81	.729
$K_{\chi}(\Delta = 20), n = 12$		
-1.9250×10^{-4}	1.9250×10^{-4}	1
-2.1650×10^{-4}	2.1650×10^{-4}	1
$-.12428$	.12428	1
$-.17073$	.17073	1
-1.4143	1.4143	1
-6.2865	6.2865	1
-66.508	66.508	1
$-37.734 \pm j60.294$	71.128	.531
-2444.1	2444.1	1
-1.0824×10^{6}	1.0824×10^{6}	1
-7.5995×10^{6}	7.5995×10^{6}	1
$K_{\mu}(\Delta = 20I_2), n = 13$		
-1.9242×10^{-4}	1.9242×10^{-4}	1
-2.1651×10^{-4}	2.1651×10^{-4}	1
-8.0876×10^{-2}	8.0876×10^{-2}	1
$-.17008$	.17008	1
$-.57388 \pm j0.77693$	.96589	.594
-1.4146	1.4146	1
-2.6054	2.6054	1
-8.2357	8.2357	1
-38.874	38.874	1
$-20.440 \pm j34.699$	40.272	.508
-202.90	202.90	1

Appendix E

Atmospheric Turbulence Model

The traditional approach to modeling atmospheric turbulence as a stochastic process has been to use the Dryden spectra. For engineering purposes it is assumed that the power spectra of atmospheric turbulence can be approximated by the Dryden spectra. (See ref. 16.) The longitudinal (body-axis) Dryden power spectrum is defined by

$$\Phi_u(\omega) = \frac{L_u}{V} \frac{2\sigma_u^2}{\pi} \frac{1}{1 + (L_u \frac{\omega}{V})^2} \tag{E1}$$

and the lateral and vertical is defined by

$$\Phi_{v,w}(\omega) = \frac{L_{v,w}}{V} \frac{\sigma_{v,w^2}}{\pi} \frac{1 + 3(L_{v,w} \frac{\omega}{V})^2}{[1 + (L_{v,w} \frac{\omega}{V})^2]^2} \tag{E2}$$

Here, V is the vehicle velocity (unit length per second) and ω is the spatial frequency and is in radians per second. The variance of the turbulence is σ^2 and the spatial scale length is L. Increasing σ scales the power spectral density (PSD) or it increases the power at all frequencies without changing the relative distribution. Changing L redistributes the power over the frequency range. Increasing the scale length of the turbulence increases the power at lower frequencies and decreases the power at higher frequencies such that the integral of the PSD remains constant; the integral of the PSD's will always equate to σ^2 for zero-mean input.

The exponents of the Dryden spectra are integers, so filters can be developed through which unit variance Gaussian white noise may be passed. The resulting filtered white noise sequence will have nearly the same statistical properties as recorded turbulence time histories.

To determine the filter equation, the following relation is used:

$$\Phi_{\text{out}} = |H(j\omega)|^2 \Phi_{\text{in}} \tag{E3}$$

where Φ_{out} is the desired Dryden spectrum, $H(j\omega)$ is the unknown filter or transfer function, and Φ_{in} is the power spectrum of the input white noise sequence. In continuous time, white noise contains all frequencies so the integral of the PSD is not defined. The magnitude of the PSD across all frequencies is prescribed to be unity. Therefore, in continuous time applications, the filters are simply the spectral roots of the Dryden spectrum equations or

$$H_u(j\omega) = \sqrt{\frac{2V\sigma_{u^2}}{L_u\pi}} \frac{1}{\frac{V}{L_u} + j\omega} \tag{E4}$$

for the longitudinal turbulence and

$$H_{v,w}(j\omega) = \sqrt{\frac{3V\sigma_{v,w^2}}{L_{v,w}\pi}} \frac{\left(\frac{V}{L_{v,w}\sqrt{3}} + j\omega\right)}{\left(\frac{V}{L_{v,u}} + j\omega\right)^2} \tag{E5}$$

for the lateral and vertical turbulence.

In the discrete time domain, as in a digital simulation, *pure* white noise cannot be generated to pass through filters; the simulation can generate frequencies only up to the Nyquist frequency. The result is a band-limited white noise sequence with a PSD that is constant but not unity. The intensity is now determined from the requirement that the integral must be the variance that is usually prescribed to be unity. Therefore, the intensity of the input noise sequence is the inverse of the Nyquist frequency or $(\Delta t)/\pi$.

The values of σ and L are tabulated in numerous references as functions of altitude and longitudinal, vertical, and lateral components. For the reference altitude used in this study (85 700 ft), the σ's and L's for longitudinal and vertical turbulence (ref. 17) (lateral was not modeled) were

$\sigma_u = 10.8$ ft/sec $\qquad \sigma_w = 6.88$ ft/sec

$L_u = 65\,574$ ft $\qquad L_w = 26\,229$ ft

With these filter parameters implemented in the Laplace domain for a discrete time simulation, the longitudinal turbulence filter becomes

$$F_u(s) = \sqrt{\frac{\pi}{\Delta t}} \sqrt{\frac{2V\sigma_{u^2}}{L_u\pi}} \frac{1}{\frac{V}{L_u} + s} \tag{E6}$$

and F_w becomes

$$F_w(s) = \sqrt{\frac{\pi}{\Delta t}} \sqrt{\frac{3V\sigma_{w^2}}{L_w\pi}} \frac{\left(\frac{V}{L_w\sqrt{3}} + s\right)}{\left(\frac{V}{L_w} + s\right)^2} \tag{E7}$$

The use of filtered white noise to represent turbulence to test or evaluate a design makes verification of correctly generated simulated turbulence necessary. For a time simulation, the output turbulence time history should be analyzed and the standard deviation of the signal should equal (to a close approximation for a sufficient number of time samples) the value used in the filter. Furthermore, the integral of any PSD of the filter output, theoretical or experimental, should equate to σ^2.

References

1. Shaughnessy, John D.; McMinn, John D.; Gregory, Irene M.; Chowdhry, Rajiv S.; Raney, David L.; and Lallman, Frederick J.: Controls, Guidance, and Trajectory Integration Issues for NASP. *Tenth National Aero-Space Plane Technology Symposium, Volume 1—Aerodynamics*, NASP CP-10060, NASP JPO, Wright-Patterson AFB, Apr. 1991, pp. 123–144.
2. Walton, James T.: Performance Sensitivity of Hypersonic Vehicles to Changes in Angle of Attack and Dynamic Pressure. AIAA-89-2463, July 1989.
3. Wilhite, Alan W.; Powell, Richard W.; Scotti, Stephen J.; McClinton, Charles R.; Pinckney, S. Zane; Cruz, Christopher I.; Jackson, L. Robert; Hunt, James L.; Cerro, Jeffrey A.; and Moses, Paul L.: Concepts Leading to the National Aero-Space Plane Program. AIAA-90-0294, Jan. 1990.
4. Cribbs, D.: Performance Uncertainty Analysis for NASP. AIAA-90-5209, Oct. 1990.
5. Shaughnessy, John D.; and Gregory, Irene M.: *Trim Drag Reduction Concepts for Horizontal Takeoff Single-Stage-To-Orbit Vehicles.* NASA TM-102687, 1991.
6. McRuer, Duane T.; Ashkenas, Irving L.; and Johnston, Donald E.: *Flying Qualities and Control Issues/Features for Hypersonic Vehicles.* NASP CR-1063, NASA JPO, Wright-Patterson AFB, 1989.
7. Anderson, Mark R.; Emami-Naeini, Abbas; Vincent, James H.: Robust Control Law Development for a Hypersonic Cruise Aircraft. *Proceedings of the 10th American Control Conference*, Volume 1, IEEE, 1991, pp. 839–845.
8. Raney, D.; and Lallman, F.: Control Concept for Maneuvering in Hypersonic Flight. AIAA-91-5055, Dec. 1991.
9. Doyle, John; Lenz, Kathryn; and Packard, Andy: Design Examples Using μ-Synthesis: Space Shuttle Lateral Axis FCS During Reentry. *Proceedings of the 25th IEEE Conference on Decision and Control*, Dec. 1986, pp. 2218–2223.
10. Jackson, Mike; and Enns, Dale: Lateral-Directional Control of an Aircraft Using μ Synthesis. AIAA-90-3412-CP, Aug. 1990.
11. Doyle, John C.; and Stein, Gunter: Multivariable Feedback Design: Concepts for a Classical/Modern Synthesis. *IEEE Trans. Autom. Control*, vol. AC-26, no. 1, Feb. 1981, pp. 4–16.
12. Doyle, John C.; Wall, Joseph E.; and Stein, Gunter: Performance and Robustness Analysis for Structured Uncertainty. *Proceedings of the 21st IEEE Conference on Decision and Control*, 1982, pp. 629–636.
13. Doyle, John C.: Structured Uncertainty in Control System Design. *Proceedings of the 24th IEEE Conference on Decision and Control*, Volume 1, 1985, pp. 260–265.
14. Shaughnessy, John D.; Pinckney, S. Zane; McMinn, John D.; Cruz, Christopher I.; and Kelley, Marie-Louise: *Hypersonic Vehicle Simulation Model: Winged-Cone Configuration.* NASA TM-102610, 1990.
15. Etkin, Bernard: Longitudinal Dynamics of a Lifting Vehicle in Orbital Flight. *J. Aerosp. Sci.*, vol. 28, no. 10, 1961, pp. 779–788.
16. Turner, Robert E.; and Hill, C. Kelly, compilers: *Terrestrial Environment (Climatic) Criteria Guidelines for Use in Aerospace Vehicle Development, 1982 Revision.* NASA TM-82473, 1982.
17. Justus, C. G.; Campbell, C. W.; Doubleday, M. K.; and Johnson, D. L.: *New Atmospheric Turbulence Model for Shuttle Applications.* NASA TM-4168, 1990.
18. Brauer, G. L.; Cornick, D. E.; and Stevenson, R.: *Capabilities and Applications of the Program To Optimize Simulated Trajectories (POST)—Program Summary Document.* NASA CR-2770, 1977.

REPORT DOCUMENTATION PAGE

Form Approved
OMB No. 0704-0188

1. AGENCY USE ONLY *(Leave blank)*

2. REPORT DATE
October 1994

3. REPORT TYPE AND DATES COVERED
Technical Memorandum

4. TITLE AND SUBTITLE
Hypersonic Vehicle Model and Control Law Development Using
H_∞ and μ Synthesis

5. FUNDING NUMBERS
WU 505-70-64-01

6. AUTHOR(S)
Irene M. Gregory, Rajiv S. Chowdhry, John D. McMinn, and
John D. Shaughnessy

7. PERFORMING ORGANIZATION NAME(S) AND ADDRESS(ES)
NASA Langley Research Center
Hampton, VA 23681-0001

8. PERFORMING ORGANIZATION REPORT NUMBER
L-17217

9. SPONSORING/MONITORING AGENCY NAME(S) AND ADDRESS(ES)
National Aeronautics and Space Administration
Washington, DC 20546-0001

10. SPONSORING/MONITORING AGENCY REPORT NUMBER
NASA TM-4562

11. SUPPLEMENTARY NOTES
Gregory, McMinn, and Shaughnessy: Langley Research Center, Hampton, VA; Chowdhry: Lockheed Engineering & Sciences Company, Hampton, VA.

12a. DISTRIBUTION/AVAILABILITY STATEMENT
Unclassified–Unlimited

Subject Category 18

12b. DISTRIBUTION CODE

13. ABSTRACT *(Maximum 200 words)*

The control system design for a single-stage-to-orbit (SSTO) air-breathing vehicle will likely be central to a successful mission because a precise ascent trajectory will preserve narrow payload margins. The air-breathing propulsion system requires that the vehicle fly in the atmosphere roughly halfway around the Earth through atmospheric turbulence. The turbulence, the high sensitivity of the propulsion system to inlet flow conditions, the relatively large uncertainty of the parameters characterizing the vehicle (due to unprecedented levels of propulsion, structural, and vehicle dynamics coupling), and the continuous acceleration make the problem especially challenging. Moreover, payload performance margins are so critical for the SSTO mission that adequate stability margins must be provided without the sacrifice of payload mass. Therefore, a modern multivariable control theory capable of explicitly including both uncertainty and performance is needed to deal with these issues. The H_∞ controller in general provides good robustness but can result in conservative solutions for practical problems involving structured uncertainty. Structured singular value μ framework for anaylsis and synthesis is potentially much less conservative in dealing with these problems and hence more appropriate for problems with tight margins. An SSTO control system requires the following: highly accurate tracking of velocity and altitude commands while limiting angle-of-attack oscillations, minimized control power usage, and a stabilized vehicle when atmospheric turbulence and system uncertainty are present. The controller designs using H_∞ and μ-synthesis procedures were compared. The mathematical model, an integrated flight/propulsion dynamic model of a conical accelerator vehicle, was linearized as the vehicle accelerated through a Mach number of 8. Vehicle acceleration through the selected flight condition gives rise to parametric variation that was modeled as a structured uncertainty. The μ analysis approach was used in the frequency domain to conduct controller analysis and was confirmed by time history plots. The results from this example demonstrate the inherent advantages of the μ framework for this class of problems.

14. SUBJECT TERMS
Robust control; Hypersonics; Control system design; Integrated flight/propulsion controls; Stuctured singular value

15. NUMBER OF PAGES
40

16. PRICE CODE
A03

17. SECURITY CLASSIFICATION OF REPORT
Unclassified

18. SECURITY CLASSIFICATION OF THIS PAGE
Unclassified

19. SECURITY CLASSIFICATION OF ABSTRACT
Unclassified

20. LIMITATION OF ABSTRACT

NSN 7540-01-280-5500

Standard Form 298(Rev. 2-89)
Prescribed by ANSI Std. Z39-18
298-102